Numerical investigation of the time-dependent stress-strain mechanical behaviour of skeletal muscle tissue in the context of Pressure Ulcer prevention

T. Lavigne[a,b,*], G. Sciumè[b], S. Laporte[a], H. Pillet[a], S. Urcun[a,b,c], B. Wheatley[d], P-Y. Rohan[a]

[a] *Arts et Metiers Institute of Technology, IBHGC, 151 bd de l'hopital, Paris, 75013, France*
[b] *Arts et Metiers Institute of Technology, Univ. of Bordeaux, CNRS, Bordeaux INP, INRAE, I2M Bordeaux, Avenue d'Aquitaine, Pessac, 33607, France*
[c] *Institute for Computational Engineering Sciences, Department of Engineering Sciences, Faculte des Sciences, de la Technologie et de Medecine, Universite du Luxembourg, Campus Kirchberg, 6, rue Coudenhove-Kalergi, Luxembourg, L-1359, Luxembourg*
[d] *Department of Mechanical Engineering, Bucknell University, 1 Dent Drive, Lewisburg, 17837, Pennsylvania, USA*

Abstract

Background: Pressure-induced tissue strain is one major pathway for Pressure Ulcer development and, especially, Deep Tissue Injury. Biomechanical investigation of the time-dependent stress-strain mechanical behaviour of skeletal muscle tissue is therefore essential to understand and prevent the onset of Deep Tissue Injury. In the literature, a viscoelastic formulation is generally assumed for the experimental characterization of skeletal muscles, with the limitation that the underlying physical mechanisms that give rise to the time dependent stress-strain behaviour are not known. The objective of this study is to explore the capability of poroelasticity to reproduce the apparent viscoelastic behaviour of passive muscle tissue under confined compression.

Methods: Experimental stress-relaxation response of 31 cylindrical porcine samples tested under fast and slow confined compression by Vaidya and collaborators were used. An axisymmetric Finite Element model was developed in ABAQUS and, for each sample a one-to-one inverse analysis was performed to calibrate the specimen-specific constitutive parameters, namely, the drained Young's modulus, the void ratio, hydraulic permeability, the

Poisson's ratio, the solid grain's and fluid's bulk moduli.
Findings: The peak stress and consolidation were recovered for most of the samples (N=25) by the poroelastic model (normalised root-mean-square error $\leq$0.03 for fast and slow confined compression conditions).
Interpretation: The strength of the proposed model is its fewer number of variables (N=6 for the proposed poroelastic model versus N=18 for the viscohyperelastic model proposed by Vaidya and collaborators). The incorporation of poroelasticity to clinical models of Pessure Ulcer formation could lead to more precise and mechanistic explorations of soft tissue injury risk factors.

Keywords: pressure ulcer, load-tolerant soft tissues, muscle passive behaviour, viscoelasticity, poroelasticity

---

Count of words. Abstract: 260; Manuscript: 3611.

1. Introduction

Pressure Ulcers (PUs) have been defined in the 2019 Clinical Practice Guideline (CPG) published jointly by the European Pressure Ulcer Advisory Panel (EPUAP), the National Pressure Injury Advisory Panel (NPIAP), and the Pan Pacific Pressure Injury Alliance (PPPIA) as *"localized injuries to the skin and underlying soft tissue that form during prolonged exposure to mechanical loads"* (Gefen et al. [1]). These usually occur over a bony prominence but may also be related to the interaction between the skin and an external medical device such as, for example, when patients interact with medical devices (orthoses, prostheses, manual wheelchair, etc) or support surfaces (Gefen et al. [2]). Despite long-standing risk assessment scales and management strategies, the relative high incidence of PUs, and especially Deep Tissue Injuries (DTI), requires extensive treatment representing a significant financial burden on health services throughout the world (Bennett et al. [3]).

Over the past 20 years, research has sought to explain soft tissue injury risk factors in terms of the local mechanical environment within soft tissues. Of particular interest are the series of experiments performed at the Eindhoven University of Technology (Ceelen et al. [4], Loerakker et al.

*Corresponding author
Email address: thomas.lavigne@ensam.eu (T. Lavigne)

[5], Stekelenburg et al. [6], van Nierop et al. [7], Traa et al. [8]) involving indentation of the tibialis anterior muscle of Brown-Norway rats that lead to identify a damage threshold for healthy murine skeletal muscle tissue. Using dedicated organ-scale Finite Element models, it was shown that direct deformation damage was apparent only when a given maximum Green-Lagrange shear strain threshold was exceeded (Ceelen et al. [4]), and that the damaged area was correlated to the magnitude of the elastic strain energy applied (Loerakker et al. [9]).

To interrogate individual soft tissue injury risk based on the evaluation of the local mechanical state, tissue-scale Finite Element models of load-bearing soft tissue in humans have been developed. These have consistently shown that bony prominence in the buttock (Linder-Ganz et al. [10, 11, 12], Luboz et al. [13], Moerman et al. [14], Macron et al. [15]), the foot (Bucki et al. [16], Niroomandi et al. [17], van Zwam et al. [18]) and at the stump-socket interface (Portnoy et al. [19], Dickinson et al. [20], Ramasamy et al. [21]) induce substantial stress concentrations (generally in skeletal muscles), which explains why these areas are vulnerable to ulceration.

Studies in the literature however are generally conducted with the assumption of quasi-static loading and response (Al-Dirini et al. [22]). Yet, the knowledge of the local mechanical condition alone is not sufficient to predict tissue damage initiation. The major limitation is that tissue damage is governed by a number of coupled biological and physical processes that occur at different spatial scales and often have very different temporal characteristics. Hence, the loading history is essential, because the time that a tissue is subjected to a sustained compression is a major determinant of tissue damage. It follows that the biomechanical investigation of the time-dependent stress-strain mechanical behaviour of soft tissues, and in particular, of skeletal muscle tissue, is essential to improve the understanding of the onset of DTI and therefore would allow a better prevention.

Attempts to characterise the time-dependence of skeletal muscle tissue generally assume a viscoelastic formulation and typically ignore the bi-phasic nature of the tissue (Van Loocke et al. [23], Simms et al. [24], Wheatley et al. [25]). In the case of viscoelasticity, the underlying physical mechanisms that give rise to the time dependent stress-strain behavior are not taken into account mechanistically. Yet, it is known that skeletal muscles are composed of a porous solid matrix (muscle fibers and extracellular matrix) filled with fluid (approximately 75% bound and free fluid Sjogaard and Saltin [26]). The overall mechanical behavior of these tissues depends not only on the solid matrix deformation, but also on the movement of the fluid within the pores during the deformation. Since fluid plays a role in the load transfer in these tissues, it follows that the stress-strain behavior of these tissues will be time dependent.

Many research teams have proposed using poroelastic constitutive models as an alternative to visco-elastic models to capture the history-dependent response of soft tissues under static and dynamics loading (Gimnich et al. [27], Argoubi and Shirazi-Adl [28], Peyrounette et al. [29], Siddique et al. [30], Hosseini-Farid et al. [31], Franceschini et al. [32], Sciumè et al. [33]). A comparison between visco-elastic and poro-elastic framework given in Appendix C. Porous media models also represent a promising approach for the integration of multiscale/multiphysics data to probe biologically relevant phenomena at a smaller scale and embed the relevant mechanisms at the larger scale (in particular, biochemistry of oxygen and of inflammatory signalling pathways), allowing the interpretation of the different time characteristics (Urcun et al. [34], Sciumè et al. [35], Sciumè [36], Gray and Miller [37], Mascheroni et al. [38]).

In a previous study, Vaidya and Wheatley [39] have tested porcine Tibialis Anterior (TA) muscle samples under fast and slow Confined/Unconfined compression and have proposed a robust hyper-viscoelastic model to numerically reproduce the mechanical behaviour in compression based on four loading conditions. Building upon this experimental work, the aim of the presented study is to explore the capability of poroelasticity to reproduce the apparent viscoelastic behaviour of passive muscle tissue under Confined Compression and to investigate the contribution of extracellular fluid flow.

2. Methods

2.1. Experimental data

This study was based on the experimental stress relaxation results of porcine muscle samples tested under fast and slow confined compression in Vaidya and Wheatley [39] (Figure 1 (a, b, c)). Briefly, thirty-one cylindrical muscle porcine samples (average height 7.03 mm and average radius 3.2 mm) were compressed in an impermeable steel well (diameter=6.9 mm, depth=8 mm), using a uniaxial tabletop Instron 3366 tensile testing system equipped with an Al2O3 porous plunger (diameter=6.4 mm, length=25.5 mm, Figure 1 (a)). Two stress relaxation testing conditions were used. Specimens were strained to 15% at two different strain rates: a fast compression at 15% s^{-1} (n=16 cylinders) and a slow compression at 1.5% s^{-1} (n=15 cylinders). They were maintained at this strain level during 400s (Figure 1 (c)). All tests were completed under transverse compression to simulate the most common uniaxial physiological loading orientation.

A visco-hyper-elastic model was calibrated in Vaidya and Wheatley [39] using unconfined and confined fast compression data concurrently. This constitutive model was based on an uncoupled Yeoh hyperelastic formulation and a four cell Maxwell viscoelastic model (four term Prony series). The results obtained are recalled in Table 1.

Law	Parameters Type	Parameter symbol	Value
Yeoh	Hyper-elastic (MPa)	$C_{10},\ C_{20},\ C_{30}$	$2.23 \cdot 10^{-5},\ 1.28 \cdot 10^{-4},\ 2.52 \cdot 10^{-5}$
	Hyper-elastic (MPa^{-1})	$D_1,\ D_2,\ D_3$	105.9, 0.839, 0.0
Prony Series	Shear Coefficients (-)	$G_1,\ G_2,\ G_3,\ G_4$	0.741, 0.086, 0.093, 0.061
	Bulk Coefficients (-)	$K_1,\ K_2,\ K_3,\ K_4$	0.563, 0.150, 0.108, 0.147
	Time Coefficients (s)	$\tau_1,\ \tau_2,\ \tau_3,\ \tau_4$	0.05, 1, 20, 400

Table 1: Hyper-elastic and viscoelastic parameters of the finite element model calibrated using unconfined and confined fast compression data concurrently [39]

The present study focuses on the Confined Compression case, but future work will extend the work to the Unconfined Compression case.

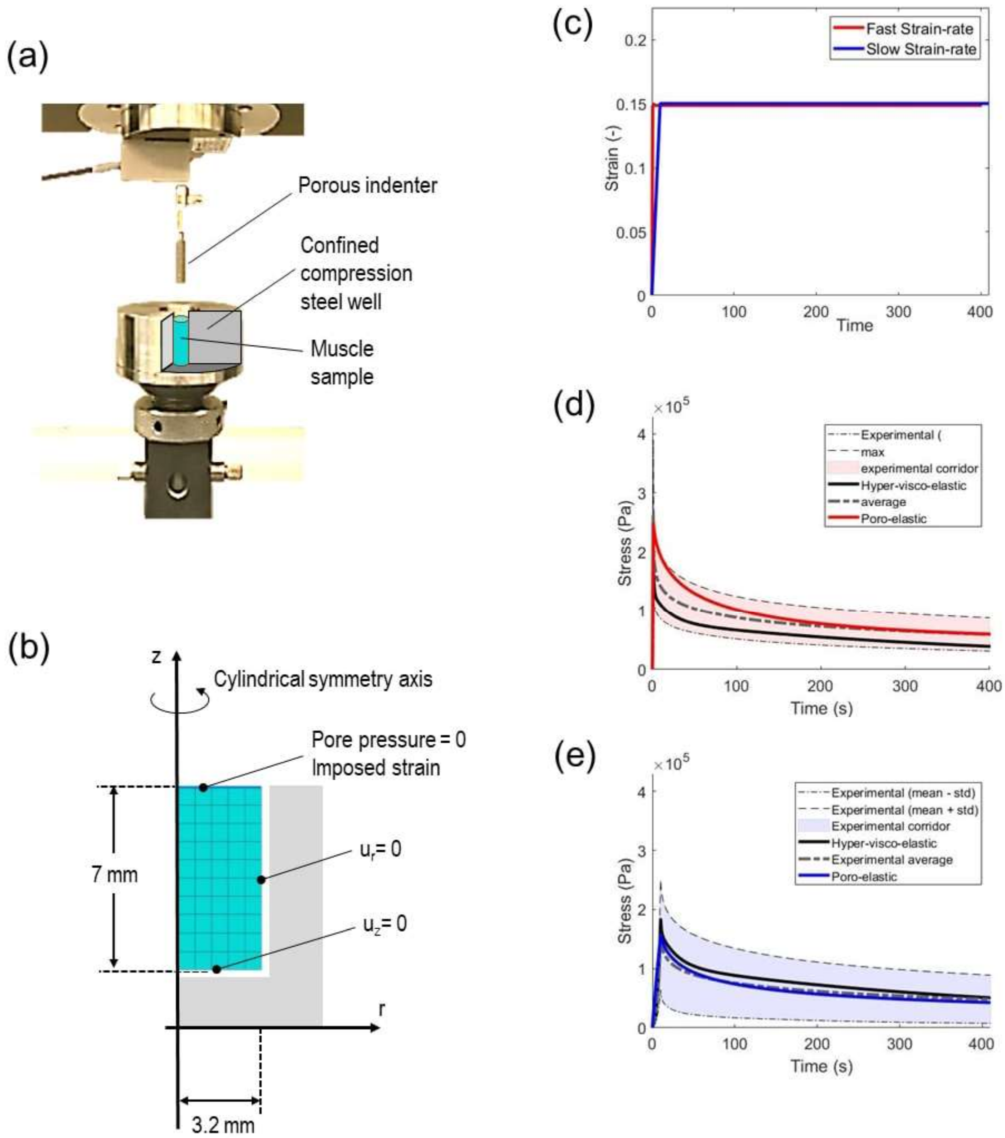

Figure 1: Experimental set up for Confined Compression (a) with its schematic representation of the finite element model (b) and imposed strain law (c) from Vaidya and Wheatley [39]. Results for the fast strain-rate (d) and for the slow strain-rate (e) average experimental relaxation curve calibration. The experimental corridor of the campaign of Vaidya and Wheatley [39] is light red for the fast strain rate and light blue for the slow one, the average experimental stress is in dashed grey. The visco-hyper-elastic model calibrated in Vaidya and Wheatley [39] is in black while poroelastic model predictions with a Poisson's ratio of 0.4879 are in red for the fast strain rate and blue for the slow strain-rate.

2.2. Finite Element Modeling

A poro-elastic mathematical model was implemented in the general purpose Finite Element software ABAQUS (ABAQUS, 2019) and an inverse analysis was performed to fit a quasi-incompressible, isotropic, poroelastic constitutive model (solid saturated by an incompressible viscous fluid) to reproduce the mean experimental mechanical response (stress relaxation). For more details on the theoretical basis of the model, the reader is refered to Appendix B. The modelling procedure folled complies with the consensus process that started within the Editorial Board of Clinical Biomechanics, and published by Viceconti and collaborators Viceconti et al. [40].

In this work, inertial and gravitational forces were neglected. It was also assumed that there is no blood flux in the samples since the experimentation was performed *ex vivo* on small samples. Muscle tissue was therefore assumed to be a mixture of two phases, an interstitial fluid and the solid scaffold. The porous medium was assumed to be fully saturated.

A preliminary study for small deformation case was carried out to assess the reliability of our formulation, comparing to the Terzaghi analytic solution (see Appendix D).

Then, a 2D axisymmetric model was proposed for the Confined Compression test (n=50 CAX4PH elements: 4-node bi-linear displacement and pore pressure, hybrid with constant pressure), as illustrated in Figure 1 (b).

The definition of the constitutive laws was defined as follows. The solid phase behaviour was assumed linear elastic (eq. B.11). Hence, it was governed by its Young's modulus, E, and Poisson's ratio, ν. The pore fluid was assumed to follow Darcy's law as presented before, and was approximated by the Foreichmer's law of Abaqus [41] (eq. 1) . Finally, the model was completed by the definition of the bulk moduli of solid grain, K^s, and of the fluid, K^l.

$$s\varepsilon^l \mathbf{v}^l = -\widetilde{k} \cdot \left(\frac{\partial \mathrm{p}}{\partial \mathbf{x}} \right) \tag{1}$$

$$\widetilde{k} = \frac{k^\varepsilon}{\mu^l} \tag{2}$$

Where $\widetilde{k}$ denotes the hydraulic permeability depending on the void ratio, $e = \frac{\varepsilon^l}{1-\varepsilon^l}$. $\mathbf{v}^l$ is the fluid velocity. Finally, p is the wetting liquid pore pressure, s the fluid saturation of the porous medium.

Boundary conditions are recalled in Figure 1 (b). As it was defined in the previous section, two types of boundary conditions were defined. Displacement BC were imposed on the top surface at the several strain rates. A pore pressure equal to zero was imposed on the fluid leaking surfaces. Displacement was vertically locked on the bottom surface and radially locked on the lateral surface.

Once the material was defined, three analysis steps were created. During the first step, only the displacement boundary conditions were defined. Additionally, an initial void ratio of the porous medium was defined. Then, the displacement load was applied during a compression step, and the pore pressure boundary condition was added. Finally, the imposed displacement was sustained so as to observe the stress relaxation during 400s. For these two last steps, the soil formulation proposed by ABAQUS was used with an iterative resolution scheme due to the high strains. The duration of the steps were provided according to Vaidya and Wheatley [39] experiments and an automatic time step was considered.

2.3. Model Calibration

The mean experimental stress relaxation curve of confined compression were fitted using the @lsqnonlin() function of Matlab (Matlab R2019a) and its 'Trust-reflective' algorithm. Specifically, we used Matlab to call ABAQUS with an initial estimate for the material model parameters, performed a forward simulation in ABAQUS, read the simulation-based output forces in Matlab, computed a custom error metric J (eq. 6) computing the error over the peak stress (eq. 3), the area between the curves (eq. 5) and the final slope of the curve (eq. 4) (over the 50 last seconds). This process was repeated iteratively until reaching the cost function local minimum.

As the algorithm 'Trust-region-reflective' of the least square minimisation function is based over gradients, it is more sensitive to the initial estimate, and a high number of parameters increase the risks of local minimums. A preliminary calibration was therefore run over the averaged stress-time experimental curve considering the 6 parameters of our model ($E,\ \nu,\ e, \tilde{k}, K^s, K^l$). In order to minimize the risk of local minimums during the calibration procedure, the following parameters were assigned the value obtained during this preliminary calibration : $\nu = 0.4879$ and $K^s = 0.799$MPa. $K^l = 2.2$GPa was assumed to be equal to the water bulk modulus. The one-to-one calibration was therefore performed on the following subset of parameters : $E,\ e, \tilde{k}$.

$$J_1 = \frac{1}{3} \cdot \left(\frac{\max(\mathbf{t}^{tot}_{abq}) - \max(\mathbf{t}^{tot}_{exp})}{\max(\mathbf{t}^{tot}_{exp})} \right)^2 \tag{3}$$

$$J_2 = \frac{1}{3} \cdot \left(\frac{\frac{\partial \mathbf{t}^{tot}_{abq}}{\partial t} - \frac{\partial \mathbf{t}^{tot}_{exp}}{\partial t}}{\frac{\partial \mathbf{t}^{tot}_{exp}}{\partial t}} \right)^2 \tag{4}$$

$$J_3 = \frac{1}{3} \cdot \left(\frac{rms(\mathbf{t}^{tot}_{abq} - \mathbf{t}^{tot}_{exp})}{norm(\mathbf{t}^{tot}_{exp})} \right)^2 \tag{5}$$

$$J = J_1 + J_2 + J_3 \tag{6}$$

Where $\mathbf{t}^{tot}_{abq}$ is the stress-time solution of ABAQUS, $\mathbf{t}^{tot}_{exp}$ is the experimental stress-time curve, $\frac{\partial \bullet}{\partial t}$ is the derivative over the last points of the data, $rms()$ and $norm()$ are respectively the root mean square and norm functions of matlab.

The samples' size, '.inp' ABAQUS files and python routines for ABAQUS are provided to the reader in Appendix A.

3. Results

3.1. Sensitivity to mesh and initial estimate

A mesh analysis was conducted. Due to the simplicity of the geometry of the sample, little variation was observed depending on the seeding. Three seeding were considered: 50 dof, 105 dof and 180 dof. These different seeding of the mesh led to negligeable change in the mechanical response (quantitatively, the cost function was unchanged and equal to 0.0061).

Another sensitivity study was carried out over the initial parameter estimates. Two initial estimates have been considered for the Young's modulus E, void ratio e and hydraulic permeability $\tilde{k}$: $[E = 17989\text{Pa}, e = 0.6996, \tilde{k} = 6.07 \cdot 10^{-14}\text{m}^2\,\text{Pa}^{-1}\,\text{s}^{-1}]$ *vs.* $[E = 8995\text{Pa}, e = 0.3498, \tilde{k} = 3.035 \cdot 10^{-14}\text{m}^2\,\text{Pa}^{-1}\,\text{s}^{-1}]$. The error metrics varied between 0.0061 and 0.0084 respectively. This difference of the cost function is discussed in the section 4.

3.2. Calibration of the average experimental relaxation curve

The result of the calibration of the average relaxation stress-time curve is superimposed in Figure 1 (d, e) onto the average experimental sample stress-time curve and the experimental corridor. The calibrated visco-hyper-elastic numerical model reported in Vaidya and Wheatley [39] is also superimposed for the ease of comparison.

The parameters identified were, respectively, for fast and slow strain-rate: Young's modulus of 22 kPa, Poisson's ratio of 0.4879, void ratio e of 0.85 (which corresponds to a porosity of 46%) and hydraulic permeability of $\tilde{k} = 4.49 \cdot 10^{-14}$ $\mathrm{m^2\,Pa^{-1}\,s^{-1}}$; Young's modulus of 5.77 kPa, Poisson's ratio of 0.4879, void ratio e of 0.64 (which corresponds to a porosity of 39%) and hydraulic permeability of $\tilde{k} = 2.33 \cdot 10^{-14}$ $\mathrm{m^2\,Pa^{-1}\,s^{-1}}$.

Quantitative error metrics of the optimisation procedure for the proposed poroelastic model are reported in Table 2. The different components of the cost function are reported, namely J_1 (eq. 3) (peak stress error), J_2 (eq. 4) (end slope error), J_3 (eq. 5) (normalised root mean square error) and J (eq. 6) (cost function). These metrics were also assessed on the numerical curves stress-time curve fitted with the visco-hyper-elastic model in Vaidya and Wheatley [39] and reported in the table for comparison. The cost function between the optimised poroelastic numerical curve and the experimental curve is smaller with the proposed poroelastic model than with the visco-hyper-elastic model in Vaidya and Wheatley [39] (0.0016 versus 0.21 for the slow and 0.0061 versus 0.2477 for the fast).

Model	Strain-rate	J_1 (eq. 3)	J_2 (eq. 4)	J_3 (eq. 5)	J (eq. 6)
Uncoupled Yeoh/Prony visco-hyper-elastic	Slow	0.0283	0.5936	0.0081	0.21
	Fast	0.1559	0.4611	0.0046	0.2477
Poro-linear-elastic Current study	Slow	0.00005	0.00079	0.0039	0.0016
	Fast	0.0026	0.0092	0.007	0.0061

Table 2: Error metrics of the average experimental stress calibrated models for the fast and slow strain-rates of the model proposed by Vaidya and Wheatley [39] and the current study's model

3.3. One to one sample calibration

The one to one calibration was carried out on n=15 samples (numbered 1 to 15) for the slow strain-rate loading condition and on n=16 samples (numbered 16 to 31) for the fast strain-rate loading condition. The corresponding stress-time curves for each sample are reported in Figures 2 and 3 respectively for the slow and for the fast loading rates. Visually inspecting the 31 calibrated curves, it can be observed that most of the samples are not fully consolidated at the end time of the experiments as the respective slope is non-zero. The calibration procedure allowed to approximate the slope between 350 s and 400 s with a poro-elastic model for all the samples (important because all the samples were not necessarily fully consolidated experimentally at 400 s). Also, the peak stress is mostly recovered by the poroelastic model (N=25/31 for which the difference between the peak stress assessed experimentally and that predicted by the simulation is lower than 5 %).

Solid Phase			Fluid Phase				Error Metrics			
Linear Elastic Law		Soil Grain Bulk Modulus	Darcy's Law			Fluid Bulk Modulus	Total	Peak Stress	Slope	RMS
E (kPa)	ν (-)	K^s (MPa)	k ($m^2\,Pa^{-1}\,s^{-1}$)	Dynamic Viscosity (Pa s)	Void ratio (-)	K^l (MPa)	J (eq. 6)	J_1 (eq. 3)	J_2 (eq. 4)	J_3 (eq. 5)
12.89 ± 11.29	0.4879	0.799	$2.09 \cdot 10^{-13} \pm 3.12 \cdot 10^{-13}$	1.0	0.469 ± 0.247	2200	0.0279 ± 0.0461	0.0175 ± 0.0285	0.0470 ± 0.1244	0.0194 ± 0.0174
20.16 ± 8.54	0.4879	0.799	$1.94 \cdot 10^{-13} \pm 5.71 \cdot 10^{-13}$	1.0	0.640 ± 0.325	2200	0.0523 ± 0.1094	0.0213 ± 0.0429	0.1005 ± 0.2582	0.0181 ± 0.0188

Table 3: Calibrated parameters and error metrics: mean and standard deviation. First line corresponds to slow-rate parameters and second line to fast-rate results

Table 3 provides the mean and standard deviation of the calibrated parameters. The parameters obtained by calibration per sample are given Appendix A. The same order of magnitude is obtained whether the strain-rate was fast or slow. The measured error metrics (eq. 6) of the calibration were respectively 0.0523 ± 0.1094 and 0.0279 ± 0.0461 (mean and standard deviation of all error metrics are provided Table 3). To quantify the goodness of fit, the value of the cost function value at the solution $\mathbf{J}^{tot}_{final}$ is given for each sample in figure 4 below.

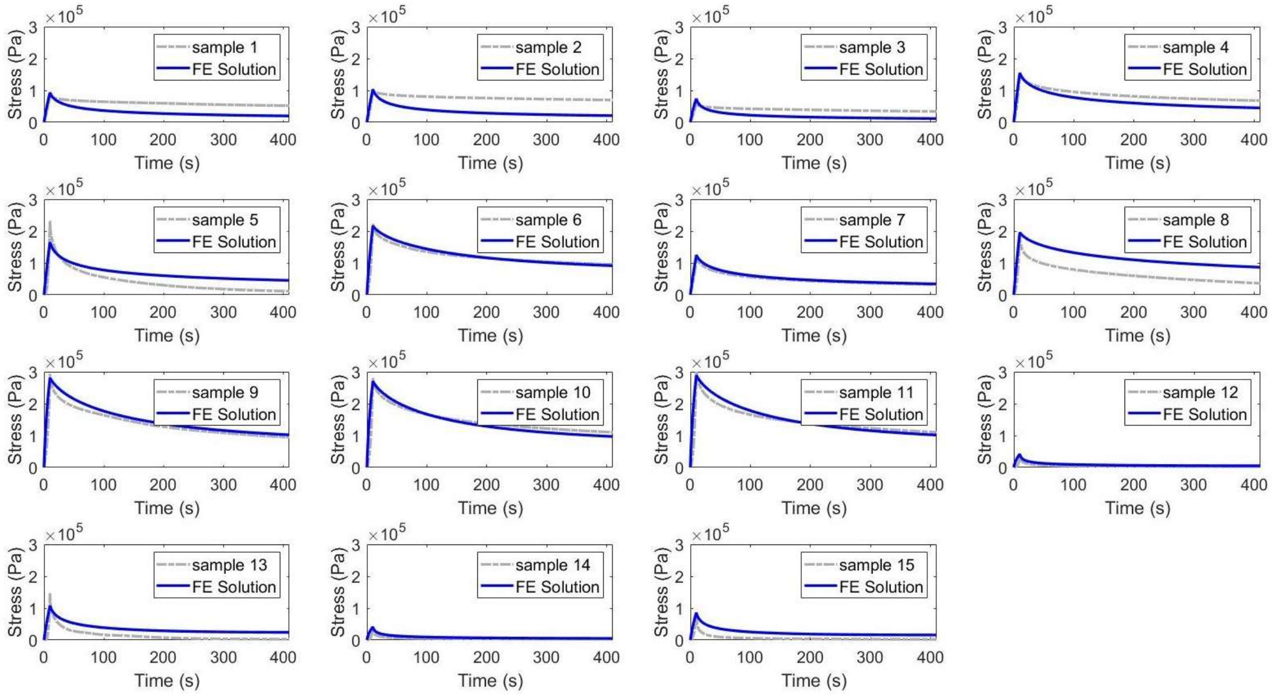

Figure 2: All 15 FE calibrated numerical solutions (blue) superimposed onto the corresponding experimental data (dashed light grey) for slow rate experiments.

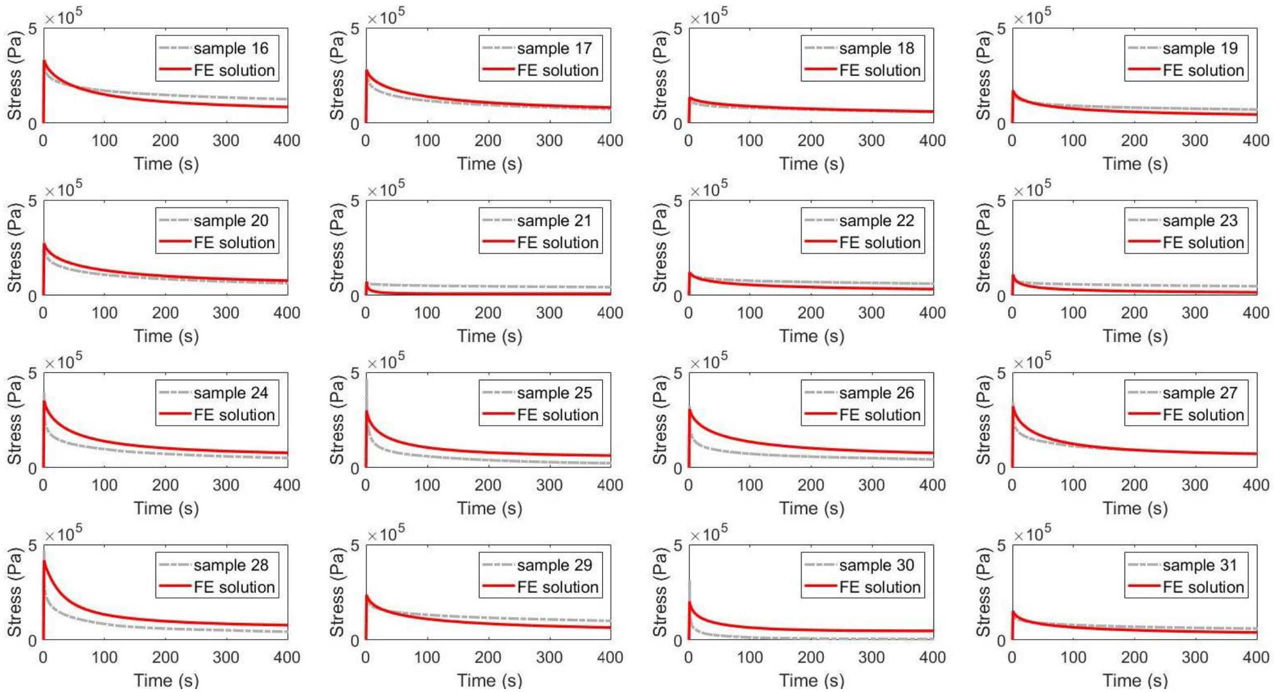

Figure 3: All 16 samples FE calibrated numerical solutions (red) superimposed onto the corresponding experimental data (dashed light grey) for fast rate experiments.

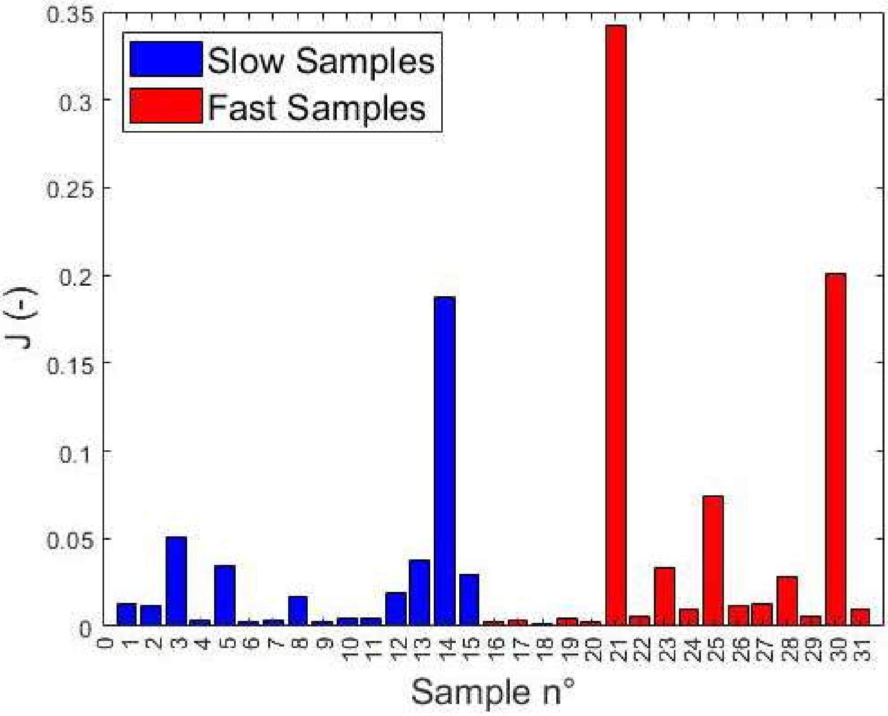

Figure 4: Cost function value at the solution for each sample. Blue corresponds to samples tested with a slow strain-rate loading and red to the samples tested with fast strain-rate loading. The proposed cost function combines the error over the peak stress, the area between the curves and the final slope (over the 50 last seconds). The cost function at the end of the identification was higher for sample 14, 21 and 30. These samples were probably already partially drained as a result of the sample preparation protocol. Hence, the assumption of full saturation might be a strong assumption.

4. Discussion

Biomechanical investigations of the time-dependent stress-strain mechanical behaviour of skeletal muscle tissue is essential to understand and proactively prevent Pressure Ulcer formation. Yet, in the literature, a viscoelastic formulation is generally assumed for the experimental characterisation of skeletal muscles, with the limitation that the underlying physical mechanisms that give rise to the time dependent stress-strain behaviour are not modelled explicitely. The objective of this study has been to explore the capability of poroelasticity to reproduce the apparent viscoelastic behaviour of passive muscle tissue under confined compression and to investigate the contribution of extracellular fluid flow. The peak stress and consolidation were recovered for most of the samples (N=25/31) by the poroelastic model (normalised root-mean-square error $\leqslant 0.03$ for fast and slow confined compression conditions).

Two strong modelling assumptions have been made for drained solid phase in this work: it was assumed to be both quasi-incompressible and linear elastic. The assumption of a quasi-incompressible drained solid phase seems reasonable because muscle fibres may exhibit nearly incompressible behaviour as fluid-filled structures with no fluid transport across the cell boundary. There is evidence that this is the case (Sleboda and Roberts [42]) and previous modeling work of muscle tissue as a multi-phase material utilized a solid phase Poisson's ratio of 0.4 (Wheatley et al. [43]). If the drained solid phase was assumed to be highly compressible, this would lead to a different set of calibrated constitutive poro-elastic parameters (the reader is referred to appendix F) strongly suggesting that further experimental and theoretical investigations are needed to shed more light on the mechanical behaviour of the drained solid scaffold.

The assumption that a linear elastic model can be used to approximate the mechanical response of the drained solid phase up to 15% of global compression is indeed a strong one considering that many studies in the literature reproduce the finite deformation of soft tissues in compression in the context of Pressure Ulcer prevention using a hyper-elastic constitutive formulation (Al-Dirini et al. [22], Moerman et al. [14], Oomens et al. [44], Traa et al. [45], Lee et al. [46], Verver et al. [47], Levy et al. [48], Linder-Ganz et al. [11], Sopher et al. [49], Zeevi et al. [50]). Yet, as demonstrated in appendix E, the hyper-elastic constitutive formulations assumed in the literature generally result in a quasi-linear stress versus strain behaviour in compression.

These results are also consistent with the results reported in Gras et al. [51] which provides evidences that a linear elastic model can be used to correctly approximate the mechanical response of tissues in confined compression (without fluid leakage). These also suggest that the main sources of non-linearities mostly come from the geometry of the samples. The large spread of estimated values of Young's modulus obtained with two loading conditions (fast or slow rate) can most probably be explained by the ill-posed nature of the inverse problem defined in this study (there is no unique solution). Future perspective work will focus on fitting stress relaxation data of muscle in both Confined Compression and Unconfined Compression.

The strength of the poroelastic model assumed in this study is the fact that we model mechanistically the phenomenon that induce the time-dependent behavior: i.e. drainage. Also, the model has a lower number of constitutive parameters compared to more complex constitutive models employed in the literature to capture the temporal evolution of muscle tissue. For example, the visco-hyper-elastic model assumed in Vaidya and Wheatley [39] has 18 parameters to calibrate versus 6 parameters in the present study: the Young's modulus and Poisson's ratio of the drained solid matrix, the void ratio and hydraulic permeability of the sample, and the soil grain's and fluid's bulk moduli. As it was the case in most of the previous studies cited, we assessed a macroscopic quasi-incompressible behaviour for the solid scaffold with a Poisson's ratio fixed to 0.4879. The identified Young's modulus were on average of 16.63 ± 10.48kPa (min: 2kPa; max: 31.19kPa) for both fast and slow rate experiments.

Few poroelastic models were previously proposed for the muscle - most of them used the poroelastic framework to model the mechanical behaviour of cartilage (Klika et al. [52]) and bone (Cowin [53], Hellmich and Ulm [54]). In experiments carried out over four New Zealand White Rabbits biceps femoris muscles, Wheatley et al. [55] identified a mean hydraulic permeability value of $7.41 \cdot 10^{-11}\mathrm{m}^2\,\mathrm{Pa}^{-1}\,\mathrm{s}^{-1}$ with a standard error of $2.2 \cdot 10^{-11}\mathrm{m}^2\,\mathrm{Pa}^{-1}\,\mathrm{s}^{-1}$. These values are higher than the calibrated values of this study (average $(2.01 \pm 4.57) \cdot 10^{-13}\,\mathrm{m}^2\,\mathrm{Pa}^{-1}\,\mathrm{s}^{-1}$, min: $7.66 \cdot 10^{-15}\,\mathrm{m}^2\,\mathrm{Pa}^{-1}\,\mathrm{s}^{-1}$; max: $2.40 \cdot 10^{-12}\,\mathrm{m}^2\,\mathrm{Pa}^{-1}\,\mathrm{s}^{-1}$) but stay close in order of magnitude from the ones we found. On the contrary, Gimnich et al. [27] reported a permeability to fluid flow $\in [3.64 \cdot 10^{-14};\ 1.27 \cdot 10^{-9}]\ \mathrm{m}^2\,\mathrm{Pa}^{-1}\,\mathrm{s}^{-1}$ if a dynamic viscosity of 1Pa s is considered.

A mean void ratio of 0.56 ± 0.3 (min: 0.092; max: 0.94) was found in this contribution. Argoubi and Shirazi-Adl [28] reported initial void ratios between 0.1 and 0.3 for bones and cartilage. Our order of magnitude is higher but is still under an equivalent porosity of 50% for the muscle tissue. This is consistent also with the observation that skeletal muscle consists of approximately 75% bound and free fluid (Sjogaard and Saltin [56]).

The calibrated results also showed some limitations of the poroelastic model used. Indeed, the toe-region of the curve did not follow the experimental curves as the initial slope is non-null. This could either be a consequence of the linear constitutive models used to represent the mechanical behaviour of both the solid scaffold (Hooke's law) and the fluids (Darcy's law) or come from experimental uncertainties (a default of parallelism between the sample and the loading plate). In the second case, the interstitial fluid would first have a lower impact on the measured reaction force, and the toe region would change. This assumption is also supported by the results of Soltz and Ateshian [57] whose experimental stress curve of the cartilage with its interstitial fluid in confined compression also has a non-null initial slope.

Although the authors had access to the experimental unconfined compression data, the authors have not been able, in this work, to numerically reproduce, in a relevant way, the boundary conditions of the experiment. This is a limitation of the current work because demonstrating that the proposed model is capable of reproducing the mechanical response of skeletal muscle tissue under different loading and boundary conditions (i.e. Confined/Unconfined Compression, slow/fast loading conditions) would further establish that poro-elasticity is sufficient to capture the underlying physical mechanisms that give rise to the time dependent stress-strain behaviour. Furture work will focus on this aspect.

Despite the limitations of the present modelling work, this contribution provides an important step toward a mechanistic interpretation of passive muscle tissue undergoing compression in the context of Deep Tissue Injury prevention. Results support the idea that the extracellular fluid contributes to the apparent viscoelastic behaviour of passive muscle tissue under confined compression. One main limitation of this work is the lack of experimental evidences on the micro-structural organisation and composition of the samples (porosity, permeability). This leads to the identification of constitutive parameters that are not unique and which affects the interpretation of the material mechanical behaviour. Further work will focus on experimental assessment of the impact of these assumptions and explore feasability of developing non-invasive methods to calibrate these parameters based on in vivo data.

Building upon recent developments on cancer modelling (Urcun et al. [34], Sciumè et al. [35], Sciumè [36], Gray and Miller [37], Mascheroni et al. [38]), a potential perspective work is to couple the current modelling framework with multiphase/mutliphysics models of bio-chemical processes responsible of the onset of Deep Tissue Injury initiation, and to assess the impact of these parameters on the mechanical response. The interplay between chemical–biological–mechanical factors is key to understand and eventually predict the initiation and propagation of soft tissue damage under extreme conditions of deformation and ischaemia. This kind of approach could be necessary in order to shed light on the relative importance (and the existence or absence of coupling according to the sub-populations at risk) of the parameters proven to be decisive in the development of pressure ulcers.

5. Conclusions

To test the hypothesis that poroelasticity is capable of reproducing the apparent viscoelastic behaviour of passive muscle tissue under confined compression, an axisymmetric Finite Element model was developed in ABAQUS. For each of the N=31 cylindrical porcine samples tested under fast and slow confined compression by Vaidya and collaborators, a one-to-one inverse analysis was performed to calibrate the specimen-specific constitutive parameters. The peak stress and consolidation were recovered for most of the samples (N=25) by the poroelastic model. The strength of the proposed model of this study is its fewer number of variables. This contribution provides an important step toward a mechanistic interpretation of passive muscle tissue undergoing compression in the context of Deep Tissue Injury prevention. Poroelasticity also represents a promising approach for integrating multi-scale/multiphysics data to probe biologically relevant phenomena at a smaller scale. The incorporation of poroelasticity to clinical models of Deep Tissue Injury formation could lead to more precise and mechanistic explorations of soft tissue injury risk factors.

6. Declaration of competing interest

Authors have no conflicts of interest to report.

7. Acknowledgment

The authors received no financial support for the research, authorship, and/or publication of this article.

Appendix A. Supplementary Data

Supplementary data to this article (.inp ABAQUS files, pre and post processing python files for ABAQUS, calibrated and raw data) can be found online.

Appendix B. Porous medium mechanics

Considering its architecture, the passive muscle tissue can be considered as a multi-phase tissue, composed by a solid scaffold and two liquid phases: the blood contained by blood vessels and the surrounding Interstitial Fluid (IF) (Sciumè [36]). With experimentation performed *ex vivo* on small samples, it was assumed that there was no blood and the model was based only on a single level of porosity with the solid scaffold, filled with IF. Also, the porous medium was assumed to be fully saturated.

In the remainder of the test, the following convention is assumed: $\bullet^s$ denotes the solid phase and $\bullet^l$ denotes the fluid phase (IF). The primary variables of the problem are the pressure applied in the pores of the porous medium and the displacement of the solid scaffold. Then, a first relationship (eq. B.1) linking the different volume fractions, can be defined. The volume fraction of the phase α is defined by (eq. B.2). ε^l is also called the porosity of the medium and is related to the void ratio, e, by eq. B.3.

$$\varepsilon^s + \varepsilon^l = 1 \tag{B.1}$$

$$\varepsilon^\alpha = \frac{\text{Volume}^\alpha}{\text{Volume}^{total}} \tag{B.2}$$

$$e = \frac{\varepsilon^l}{1 - \varepsilon^l} \tag{B.3}$$

Assuming that there is no inter-phase mass transport, the spatial form of the mass balance equation of the solid and liquid phase is respectively then given by equations (eq. B.4) and (eq. B.5).

$$\frac{\text{D}^s}{\text{D}t}(\rho^s\varepsilon^s) + \rho^s\varepsilon^s\nabla\cdot\mathbf{v}^\mathbf{s} = 0 \tag{B.4}$$

$$\frac{\text{D}^s}{\text{D}t}(\rho^l\varepsilon^l) + \nabla\cdot(\rho^l\varepsilon^l(\mathbf{v}^l - \mathbf{v}^s)) + \rho^l\varepsilon^l\nabla\cdot\mathbf{v}^\mathbf{s} = 0 \tag{B.5}$$

Where $\frac{D^s}{Dt}$ is the particle derivative with respect to the movement of the phase $\bullet^s$, $\mathbf{v}^\alpha$ is the local velocity vector of the phase α and ρ^α the density of the phase α.

Using (eq. B.1), (eq. B.4) gives:

$$\frac{D^s}{Dt}(\rho^s(1-\varepsilon^l)) + \rho^s(1-\varepsilon^l)\nabla \cdot \mathbf{v^s} = 0 \tag{B.6}$$

For the fluid phase, Darcy's law (eq. B.7) is used to evaluate the fluid flow in the porous medium.

$$\varepsilon^l(\mathbf{v}^l - \mathbf{v}^s) = -\frac{k^\varepsilon}{\mu^l}(\nabla \mathrm{p} - \rho^l \mathbf{g}) \tag{B.7}$$

Where k^ε is the intrinsic permeability (m^2), μ^l is the dynamic viscosity (Pa s), p the pressure and $\mathbf{g}$ the gravity. $\frac{k^\varepsilon}{\mu^l}$ is called the hydraulic permeability.

Then, (eq. B.7) is injected in (eq. B.5) as follows:

$$\frac{D^s}{Dt}(\rho^l\varepsilon^l) - \nabla \cdot (\rho^l(\frac{k^\varepsilon}{\mu^l}(\nabla \mathrm{p} - \rho^l \mathbf{g})) + \rho^l\varepsilon^l\nabla \cdot \mathbf{v^s} = 0 \tag{B.8}$$

$$\iff \frac{D^s}{Dt}(\rho^l\varepsilon^l) - \nabla \cdot \rho^l(\nabla(\frac{k^\varepsilon}{\mu^l}\mathrm{p})) + \nabla \cdot (\rho^l\frac{k^\varepsilon}{\mu^l}\mathbf{g}) + \rho^l\varepsilon^l\nabla \cdot \mathbf{v^s} = 0 \tag{B.9}$$

Concerning the mechanical constitutive model, similarly to what was proposed by Terzaghi for a 1D consolidation (Appendix C.1), an effective stress tensor denoted $\mathbf{t}^{eff}$ is responsible for all deformation of the solid ECM scaffold. Hence the total stress tensor is defined by (eq. B.10).

$$\mathbf{t}^{tot} = \mathbf{t}^{eff} - \beta \mathrm{p} \mathbf{I_d} \tag{B.10}$$

Where β is the Biot's coefficient and $\mathbf{I_d}$ is the identity matrix.

Assuming linear elastic behaviour, the effective stress tensor is defined by (eq. B.11).

$$\mathbf{t}^{eff} = \mathbf{C} : \mathbf{d} \tag{B.11}$$

Then, applying the conservation of momentum, the governing equations of this one level porous medium are:

$$\frac{\mathrm{D}^s}{\mathrm{D}t}(\rho^s(1-\varepsilon^l)) + \rho^s(1-\varepsilon^l)\nabla\cdot\mathbf{v^s} = 0 \qquad \text{(B.12)}$$

$$\frac{\mathrm{D}^s}{\mathrm{D}t}(\rho^l\varepsilon^l) - \nabla\cdot\rho^l(\nabla(\frac{k^\varepsilon}{\mu^l}\mathrm{p})) + \nabla\cdot(\rho^l\frac{k^\varepsilon}{\mu^l}\mathbf{g}) + \rho^l\varepsilon^l\nabla\cdot\mathbf{v^s} = 0 \qquad \text{(B.13)}$$

$$\nabla\cdot(\mathbf{t}^{tot}) + f_v = \rho^s\gamma^s \qquad \text{(B.14)}$$

Where f_v are the force densities applied to the medium and γ^s is the acceleration of the solid phase.

Three boundaries were defined: the first one, Ω_u has imposed displacement (eq. B.15), the second one Ω_s has imposed external forces (eq. B.16) and Ω_p is submitted to an imposed pressure (fluid leakage condition (eq. B.17)). We obtain:

$$\mathbf{t}^{eff} = \mathbf{t}^{imposed} \text{ on } \Omega_s \qquad \text{(B.15)}$$

$$\mathbf{u}^s = \mathbf{u}^{imposed} \text{ on } \Omega_u \qquad \text{(B.16)}$$

$$p = 0 \text{ on } \Omega_p \qquad \text{(B.17)}$$

Appendix C. Poroelasticity to capture the time-dependent response of muscle

Most of biological soft tissues has a porous/fibrous nature consisting of a solid scaffold giving mechanical stability and one or more fluid or pseudo-fluid phases which saturate the porosity. Hence, to mechanistically model a biological human (or animal) tissue accounting for the interaction between the solid matrix (primarily constituted by proteins and collagen fibers) and the fluid phases one must use porous media mechanics. Despite this consciousness, researchers are still today much more used to employ viscoelasticity to model the time-dependent behavior of soft tissues. If on one hand its is true that viscoelastic models are typically very effective to fit usual experimental tests, however the underlying physical mechanisms that give rise to the time-stress dependent behavior is not well known and found material parameters may vary with the considered boundary conditions.

Lets we consider two reference models: i) a two-phase (one solid-one fluid) poroelastic model and ii) a rheological viscoelastic model constituted by a

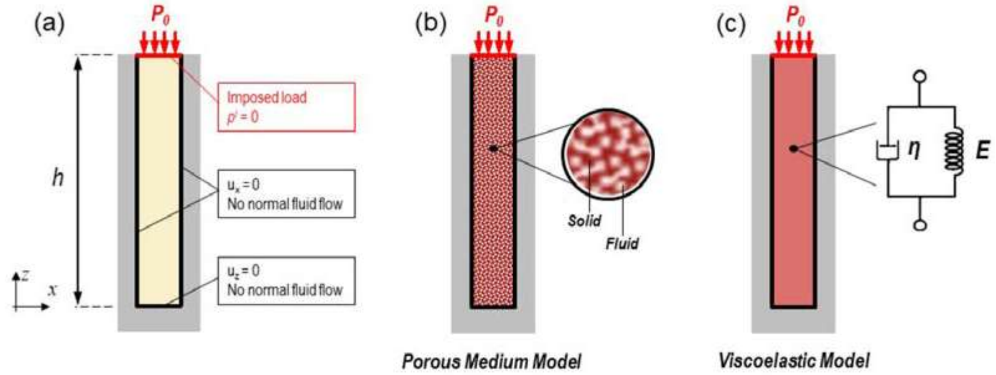

Figure C.5: One dimensional consolidation. (a) Geometry and boundary conditions; (b-c) porous medium and viscoelastic models

Kelvin-Voight chain; and use these two models to simulate a 1D confined compression test. In this test the tissue is constrained in a cylindrical or prismatic chamber and compressed at the top surface with a constant pressure, p_0. The specimen is fully sealed with the exception of the top surface where a porous membrane allows drainage of the inside fluid during the test. The geometry and boundary conditions of the test are represented in Figure C.5. This kind of test, which takes up the paradigms of one of the most important characterization essay in soil mechanics (it is named oedometer test or 1D consolidation test), is a very frequent test performed to characterize the dynamics response of biological soft tissue.

Appendix C.1. Terzaghi's analytic solution

The Terzaghi analytical solution given by (eq. C.1) gives the solution to 1D porous medium mechanics a series expansion function of the 1D-coordinate. Hereunder are recalled the hypotheses of the Terzaghi's solution (Tavenas, F. et al. [58]):

1. the sample is submitted to small and unidirectional strains
2. The solid grains and fluid are supposed in-compressible
3. The material is homogeneous
4. The mechanical parameters stay constant during all the settlement
5. The fluid leakage is unidirectional and follows the Darcy's law

6. There is a linear law between the effective stresses and volume variation of the soil
7. The soil has no structural viscosity or secondary settlement

$$\text{p} = \frac{4p_0}{\pi} \sum_{k=1}^{+\infty} \frac{(-1)^{k-1}}{2k-1} \cos[(2k-1)\frac{\pi}{2}\frac{z}{h}] \exp[-(2k-1)^2 \frac{\pi^2}{4}\frac{c_v t}{h^2}] \tag{C.1}$$

$$c_v = \frac{k^\varepsilon}{\mu^l (S + \frac{\beta^2}{M})} \tag{C.2}$$

$$M = \frac{3K^s(1-\nu)}{(1+\nu)} \tag{C.3}$$

$$S = \frac{\beta - \varepsilon_0^l}{K^s} + \frac{\varepsilon_0^l}{K^l} \tag{C.4}$$

Where p_0 is the full applied load, z is the altitude, h is the initial height of the sample , c_v is the consolidation coefficient defined by (eq. C.2), M the longitudinal modulus (eq. C.3), K^α the bulk's modulus of the α phase, ν the Poisson's ratio, S the inverse of the Biot Modulus (eq. C.4), β is the Biot coefficient and ε_0^l is the initial porosity.

Looking to (eq. C.1), a consolidation time $T_v = \frac{h^2}{c_v}$ was defined. Ususally, in the assumption of a compressibility of the phases larger than the porous medium compressibility, then $\beta = 1$ and $S = 0$ gives:

$$c_v = \frac{k^\varepsilon M}{\mu^l} \tag{C.5}$$

$$T_v = \frac{h^2 \mu^l}{k^\varepsilon M} \tag{C.6}$$

The consolidated stress, $t^{consolidated}$ was also computable (eq. C.7),

$$t^{consolidated} = M \frac{u_{imposed}}{h} \tag{C.7}$$

Where $u_{imposed}$ is the imposed displacement on the top surface and h is the initial height of the sample.

So in this minimal version of porous medium model the behaviour is governed by three parameters: the elastic coefficients E and ν (which determine

M) and the ratio between the intrinsic permeability of the solid and the dynamic viscosity of the fluid $\frac{k}{\mu^l}$. From eq. C.1 quasi-analytical solutions can be derived for the vertical strain and vertical displacement along the vertical coordinate.

Appendix C.2. Viscoelastic formulation

The analytical solution of the viscoelastic model has a much simpler form and gives the vertical displacement of the points along the vertical coordinate of the column as a function of time

$$u_z(z,t) = -\frac{p_0\,t}{M}[1 - \frac{E\,t}{\eta}] \tag{C.8}$$

So also in this model the behaviour is governed by three parameters: the elastic coefficients E (stiffness of the spring in the 1D rheological model) and ν and the viscosity of the damper η.

Appendix C.3. Comparison between the two solutions

For the simulated experiment the column height, h is of 1 cm and the pressure, p_0, imposed at the top of the column is equal to 10 Pa. For the porous medium formulation the following parameters are assumed: Young's modulus E equal to 1 kPa; Poisson's ration ν equal to 0.4; intrinsic permeability of the solid scaffold, k, equal to 4×10^{-16} m^2; and dynamic viscosity of the fluid, μ^l, equal to 0.001 Pa s. For the viscoelastic model the Young's modulus and the Poisson's ratio have the same values of the porous medium model. For the viscosity of the damper, η, a value of 4.4×10^7 Pa s has been identified which, for h equal to 1 cm, gives an overall response in term of vertical displacement of the top point very similar to that of the porous medium model (see Figure C.6.d solid lines). In this figure we can observe that the initial agreement between the two formulations is not optimal; however, after 24 hours the two curves are superposed. To better understand the behaviour of the two models we can analyse more in depth such results by plotting the vertical displacement along the vertical coordinate at different times for the porous medium and the viscoelastic models. In Figure C.6.c we can observe that in the porous medium model the displacement in proximity of the drying surface grows initially more rapidly than in the viscoelastic case since this area is rapidly consolidated in the first phase of the compression process. This can be more easily understood looking at Figure C.6.b which shows the fluid pressure along the vertical coordinate at different times for the porous medium model. We can observe that the pressure decreases progressively over the time due to the consolidation process.

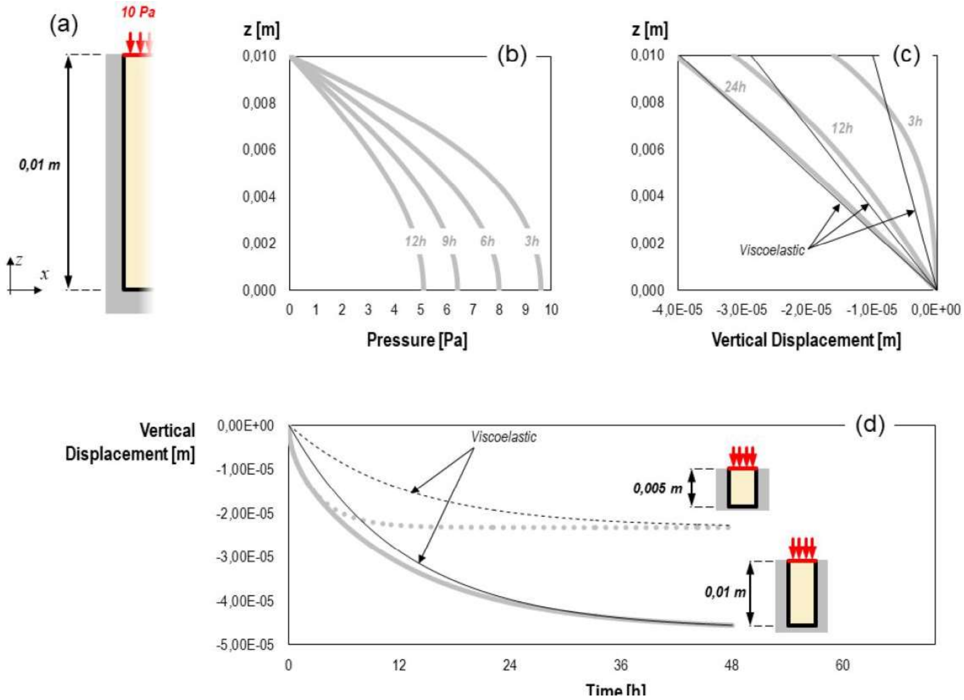

Figure C.6: Results for the 1D consolidation case. (a) Specimen geometry. (b) Fluid pressure along the vertical coordinate at different times (porous medium model). (c) Vertical displacement along the vertical coordinate at different times for the porous medium model (gray line) and the viscoelastic model (black line). (d) Vertical displacement of the top surface versus time for the porous medium model (gray line) and the viscoelastic model (black line); two cases are considered: h = 1 cm (solid lines) and h = 0.5 cm (dashed lines).

Hence, this initial heterogeneity of strain along the vertical coordinated cannot be reproduced with the viscoelastic model since the drainage of the fluid is not explicitly modelled. However, the worst is still to come. Let's we consider now a column with h equal to 0:5 cm, one half of the previously assumed height. The overall vertical displacement of the top surface is depicted in Figure C.6.d. for the porous medium (gray dashed line) and viscoelastic (black dashed line) models. The figure shows that this time the dynamics is fully different. In the porous medium case the column consolidates much faster than in the viscoelastic case. If we compare the solution of $h = 0.5$ cm (dashed lines) with those of $h = 1$ cm (solid lines) we see that the dynamics of the visocelastic model remains the same (obviously with a different asymptotic tendency) while the porous medium model consolidates almost four time faster for $h = 0.5$ cm. To decipher the reason of the discordance between solutions of the viscoelastic and porous medium models one can consider the unit of the factors that drive time dependent response in the two cases. Looking firstly at the analytical solution of the viscoelastic model from eq. C.8 we deduce that the characteristic time of the consolidation process is proportional to $\frac{\eta}{E}$ (that quantity has the dimension of a time). In the porous medium model the time dependent response is governed by the consolidation coefficient and the characteristic time of the consolidation process is proportional to $\frac{h^2}{c_v}$ (eq. C.6) and that therefore the length of the drainage path h has a capital impact on the consolidation dynamics. From these analyses we deduce that for the porous medium model once parameter are identified these remain suitable also in other experimental situations. Conversely, if we want to mimic the behaviour of a porous material with a viscoelastic model we must adjust the parameter η accounting for the specimen size and boundary conditions. If on one hand this is feasible for a 1D case, on the other hand we can imagine that could be very difficult for more complex configurations.

Appendix D. Terzaghi's analytic solution with Abaqus

For the confined compression tests, the expected result was similar to a 1D compression. Hence, the Terzaghi analytical solution given by (eq. C.1) was used to assess the reliability of the ABAQUS model considered. The analytical solution is recalled section Appendix C.1.

Solid Phase			Fluid Phase			
Linear Elastic Law		Soil Grain Bulk Modulus	Darcy's Law			Fluid Bulk Modulus
E (kPa)	ν (-)	K^s (MPa)	k ($m^2\,Pa^{-1}\,s^{-1}$)	Dynamic Viscosity (Pa s)	Void ratio (-)	K^l (MPa)
1.0	0.4	0.001 (full line) /2200 (dashed line)	$4 \cdot 10^{-13}$	1.0	1.0	2200

Table D.4: Parameters used in the verification model

According to section 2.2, a preliminary study was carried out over a small strain model. A 2D axi-symmetric ABAQUS model composed of (n=60 CAX4PH elements) of an imposed load experiment was proposed. An imposed pressure of 10 Pa was applied on the top surface and boundary conditions are presented Figure C.5. The material parameters are given Table D.4. Two different conditions were tested: $K^s = 0.001\text{MPa} \implies \beta =$

$1 - \frac{E}{3K^s(1-2\nu)} = 0.83$ which is lower than the soil bulk modulus expected for the muscle and $K^s = 2.2e9\text{MPa} \implies \beta = 1 - \frac{E}{3K^s(1-2\nu)} \approx 1.0$ which allowed to be closer to the assumption 2 above.

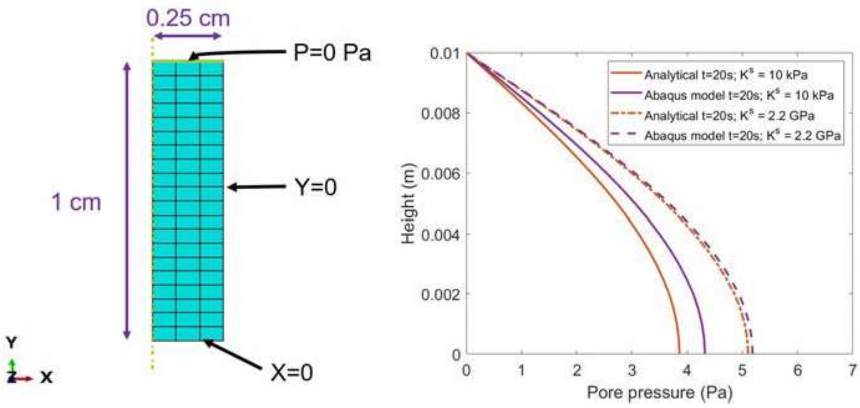

Figure D.7: Discretized Finite Element model (left) and comparaison to the analytical solution (right)

The result obtained are presented on the right of Figure D.7. The dashed curves correspond to the quasi-incompressible soil grains and plain curves to the non-incompressible soil grain model. As expected, the quasi-incompressible soil grains' curve was quasi-super-imposed. There was a difference for the non-incompressible soil grain, probably because the hypotheses were not fully covered but the order of magnitude was good.

Finally, as our samples were submitted to high strains, the use of the analitycal solution was not possible to directly model the available experimental data.

Appendix E. Hyper-elasticity models for the buttock tissue

To quantitatively assess the influence of the assumed constitutive law when simulating the finite deformation of soft tissue in compression in the context of Pressure Ulcer prevention, a the semi-confined compression experiment is simulated (Figure E.8 below). The numerical experiment consists in testing in compression a cylindrical specimen with low-aspect ratio. In the semi-confined configuration, the top and bottom faces of the specimen are rigidly attached to the platens of the stress–strain machine to ensure no-slip boundary conditions.

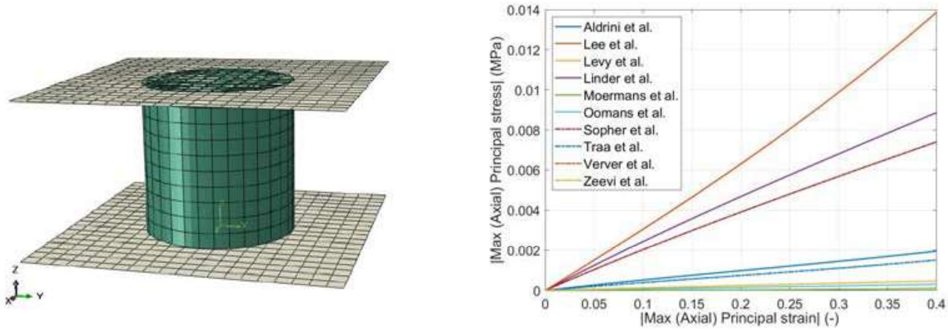

Figure E.8: Numerical model of the semi-confined experiment proposed (left) and resulting stress-strain curves (right). The references of the legend correspond to the ones of Table E.5

The constitive laws found in the litterature are mostly variation around three main strain-energy density functions : Ogden Law (E.1), Mooney-Rivlin and Neo-Hookean (E.3). The Mooney-Rivlin is computed in abaqus as a generalized Rivlin model with one mode (E.2). For each equation, W is the strain energy density function, $\bar{\lambda}_i$ are the deviatoric stretches, $\bar{I}_i$ are the deviatoric invariants of the Green-Cauchy left transformation tensor and J the Jacobian of the transformation tensor.

$$W(\bar{\lambda}_i) = \frac{\mu_1}{\alpha_1}(\sum_i \bar{\lambda}_i^{\alpha_1} - 3) + \frac{1}{D_1}(J-1)^2 \tag{E.1}$$

$$W(\bar{I}_i) = C_{10}(\bar{I}_1 - 3) + C_{01}(\bar{I}_2 - 3) + \frac{1}{D_1}(J-1)^2 \tag{E.2}$$

$$W(\bar{I}_i) = C_{10}(\bar{I}_1 - 3) + \frac{1}{D_1}(J-1)^2 \tag{E.3}$$

Some articles used different forms of those equations but due to the assumption of incompressibility, all those writings are equivalent. We computed the equivalent parameters to be used in ABAQUS. The table E.5 presents for each article the considered constitutive law and the parameters used in ABAQUS. As ABAQUS uses pre-encoded equation, the parameters or the equation formulation can be simplified or slightly modified in regard of the one used in the articles.

Looking to Figure E.8, the hyper-elastic laws with their associated parameters for muscle tissue may be, at least during the 15 first percent of compression, approximated by a linear-elastic law for the solid scaffold.

Appendix F. Poroelastic model parameter identification assuming a highly compressible drained solid phase (Poisson's ratio of 0.2)

Appendix F.1. Calibration of the average experimental relaxation curve

Similarly to the previous section, the result of the calibration of the average relaxation stress-time curve is superimposed in Figure F.9 onto the average experimental sample stress-time curve and the experimental corridor. The calibrated visco-hyper-elastic numerical model reported in Vaidya and Wheatley [39] is also superimposed for the ease of comparison.

The parameters identified were, respectively, for fast and slow strain-rate: Young's modulus of 149 kPa, Poisson's ratio of 0.2, void ratio e of 1.0 (which corresponds to a porosity of 50%) and hydraulic permeability of $k = 2.32 \cdot 10^{-14}\ \mathrm{m^2\,Pa^{-1}\,s^{-1}}$; Young's modulus of 99.3 kPa, Poisson's ratio of 0.2, void ratio e of 0.72 (which corresponds to a porosity of 42%) and hydraulic permeability of $k = 4.16 \cdot 10^{-14}\ \mathrm{m^2\,Pa^{-1}\,s^{-1}}$.

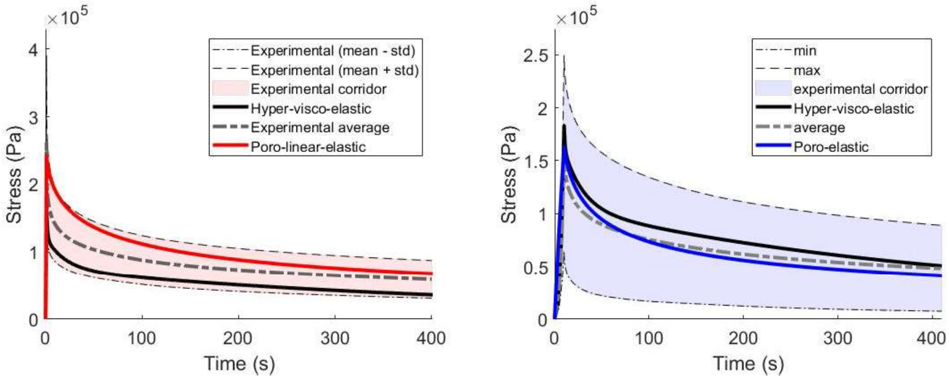

Figure F.9: Results for the fast strain-rate (left) and for the slow strain-rate (right) average experimental relaxation curve calibration. The experimental corridor of the campaign of Vaidya and Wheatley [39] is light red for the fast strain rate and light blue for the slow one, the average experimental stress is in dashed grey. The visco-hyper-elastic model calibrated in Vaidya and Wheatley [39] is in black while poroelastic model predictions with a Poisson's ratio of 0.2 are in red for the fast strain rate and blue for the slow strain-rate.

Quantitative error metrics of the optimisation procedure for the proposed poro-linear-elastic model are reported in Table F.6. The different components of the cost function are the same than section 3. These metrics were also assessed on the numerical curves stress-time curve fitted with the visco-hyper-elastic model in Vaidya and Wheatley [39] and reported in the table for the sake comparison. The cost function between the optimised poroelastic numerical curve and the experimental curve is smaller with the proposed poroelastic model than with the visco-hyper-elastic model in Vaidya and Wheatley [39] (0.0022 versus 0.21 for the slow and 0.0375 versus 0.2477 for the fast).

Appendix F.1.1. One to one sample calibration

The one to one calibration was carried out on the n=16 samples for fast strain-rate and n=15 samples for slow strain-rate. The corresponding stress-time curves for each sample are reported in Figures F.10 and F.11 respectively for the slow and for the fast loading rates. Looking to the 31 calibrated curves, the slope between 350 s and 400 s is mostly approximated: most of the samples are not fully consolidated at the end time of the experiments as the slope is non-null. Also the peak stress is mostly recovered by the poroelastic model.

Article	Constitutive Law	ABAQUS Parameters
Al-Dirini et al. [22]	Ogden	$\mu_1 = 1.91e-3$MPa $\alpha_1 = 4.6$ $D_1 = 9.179$MPa^{-1}
Lee et al. [46]	Moonley-Rivlin	$C_{01} = 1.65e-3$MPa $C_{10} = 3.35e-3$MPa $D_1 = 4.03$MPa^{-1}
Levy et al. [48]	Neo-Hookean	$D_1 = 2.83$MPa^{-1} $C_{10} = 3.55e-3$MPa
Linder-Ganz et al. [11]	Neo-Hookean	$D_1 = 1.18$MPa^{-1} $C_{10} = 4.25e-3$MPa
Moerman et al. [14]	Ogden	$\mu_1 = 5.575e-4$MPa $\alpha_1 = 12$ $D_1 = 7.47$MPa^{-1}
Oomens et al. [44]	Ogden	$\mu_1 = 3.0e-4$MPa $\alpha_1 = 5$ $D_1 = 13.36$MPa^{-1}
Sopher et al. [49]	Neo-Hookean	$D_1 = 2.817$MPa^{-1} $C_{10} = 3.55e-3$MPa
Traa et al. [45]	Ogden	$\mu_1 = 1.49e-3$MPa $\alpha_1 = 5$ $D_1 = 57$MPa^{-1}
Verver et al. [47]	Moonley-Rivlin	$C_{01} = 1.65e-3$MPa $C_{10} = 3.35e-3$MPa $D_1 = 5.04$MPa^{-1}
Zeevi et al. [50]	Neo-Hookean	$D_1 = 53.3$MPa^{-1} $C_{10} = 2.25e-3$MPa

Table E.5: Table gathering all the considered articles and their associated parameters used in ABAQUS

Model	Strain-rate	J_1 (eq. 3)	J_2 (eq. 4)	J_3 (eq. 5)	J (eq. 6)
Uncoupled Yeoh/Prony visco-hyper-elastic	Slow	0.0283	0.5936	0.0081	0.21
	Fast	0.1559	0.4611	0.0046	0.2477
Poro-linear-elastic Current study	Slow	0.0014	0.00055	0.0046	0.0022
	Fast	0.0056	0.0974	0.0093	0.0375

Table F.6: Error metrics of the average experimental stress calibrated models for the fast and slow strain-rates of the model proposed by Vaidya and Wheatley [39] and the current study's model

Solid Phase			Fluid Phase				Error Metrics			
Linear Elastic Law		Soil Grain Bulk Modulus	Darcy's Law			Fluid Bulk Modulus	Total	Peak Stress	Slope	RMS
E (kPa)	ν (-)	K^s (MPa)	k ($m^2\,Pa^{-1}\,s^{-1}$)	Dynamic Viscosity (Pa s)	Void ratio (-)	K^l (MPa)	J (eq. 6)	J_1 (eq. 3)	J_2 (eq. 4)	J_3 (eq. 5)
116.02 ± 31.89	0.2	0.799	$1.16 \cdot 10^{-12} \pm 1.93 \cdot 10^{-12}$	1.0	0.81 ± 0.24	2200	0.121 ± 0.161	0.0167 ± 0.0228	0.322 ± 0.472	0.024 ± 0.022
133.75 ± 24.54	0.2	0.799	$1.87 \cdot 10^{-12} \pm 4.17 \cdot 10^{-12}$	1.0	0.95 ± 0.11	2200	0.12 ± 0.13	0.069 ± 0.086	0.422 ± 0.269	0.016 ± 0.0105

Table F.7: Calibrated parameters and error metrics: mean and standard deviation. First line corresponds to slow-rate parameters and second line to fast-rate results

Table F.7 provides the mean and standard deviation of the calibrated parameters. The same order of magnitude is obtained whether the strain-rate was fast or slow. The measured error metrics of the calibration were respectively 0.12 ± 0.13 and 0.121 ± 0.161 (mean and standard deviation of all error metrics are provided Table F.7). Once again, these results support the apparent capacity of the model to mostly capture the peak stress and relaxation described previously also minimising the root mean square error metric.

To quantify the goodness of fit, the value of the cost function value at the solution $\mathbf{J}^{tot}_{final}$ is given for each sample in figure F.12 below.

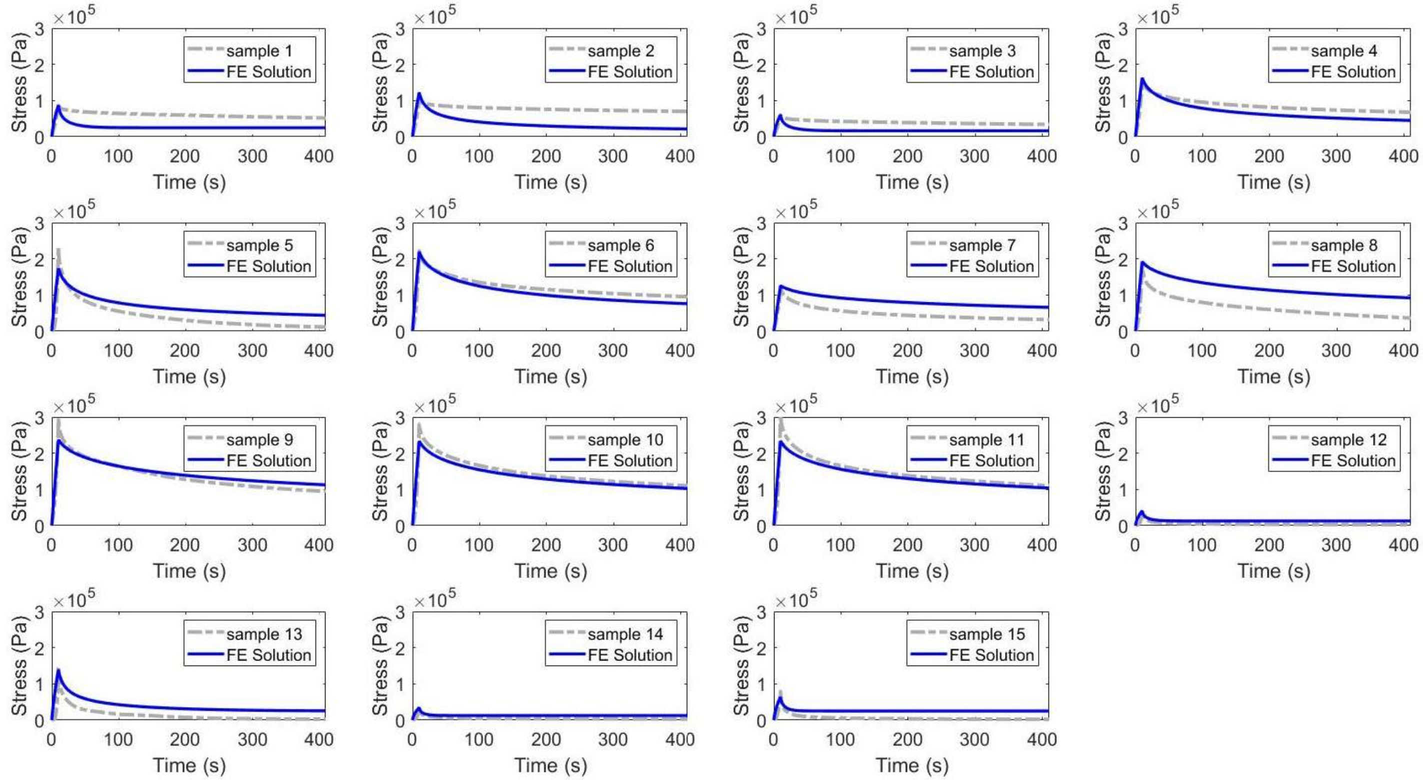

Figure F.10: All 15 FE samples calibrated models (blue) superimposed with the corresponding experimental data (light grey) for slow rate experiment

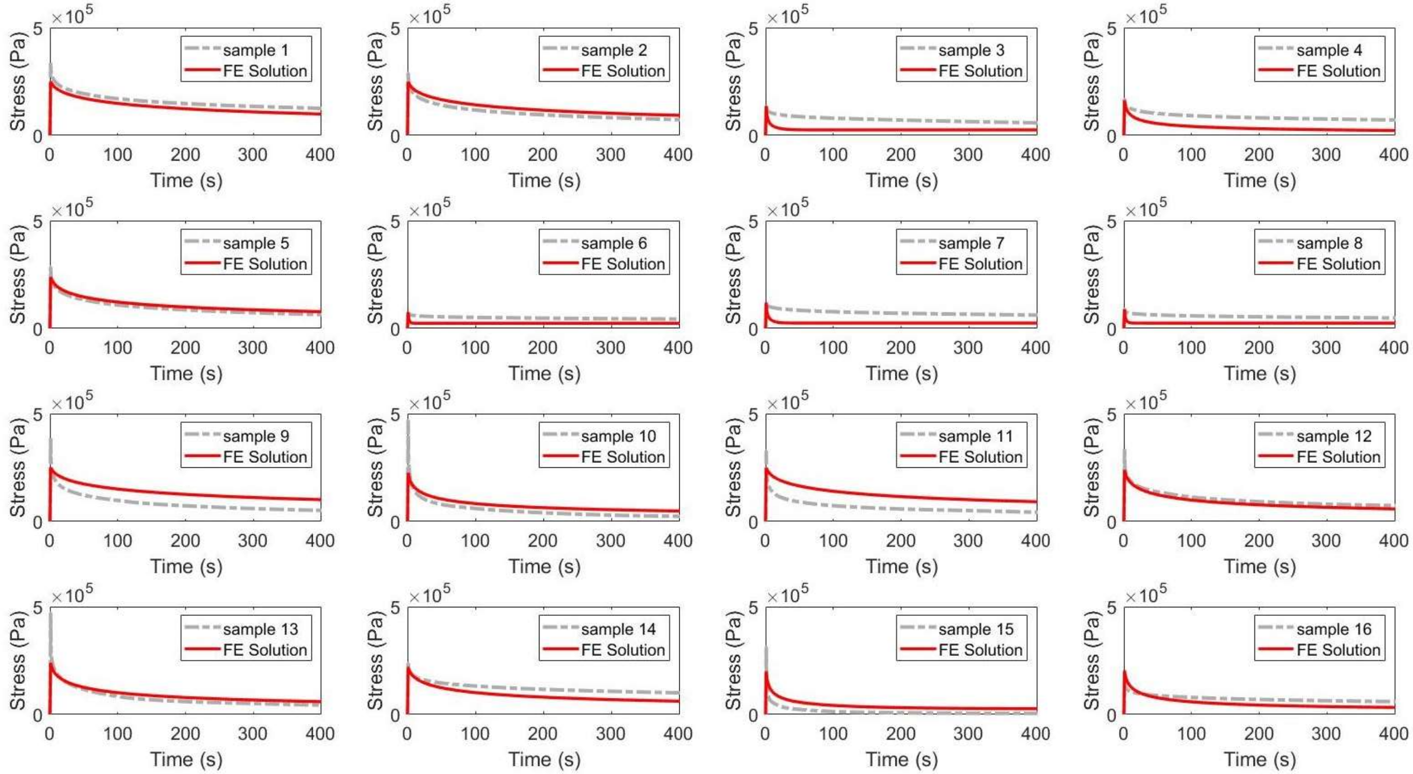

Figure F.11: All 16 samples FE calibrated models (red) superimposed with the corresponding experimental data (light grey) for fast rate experiment

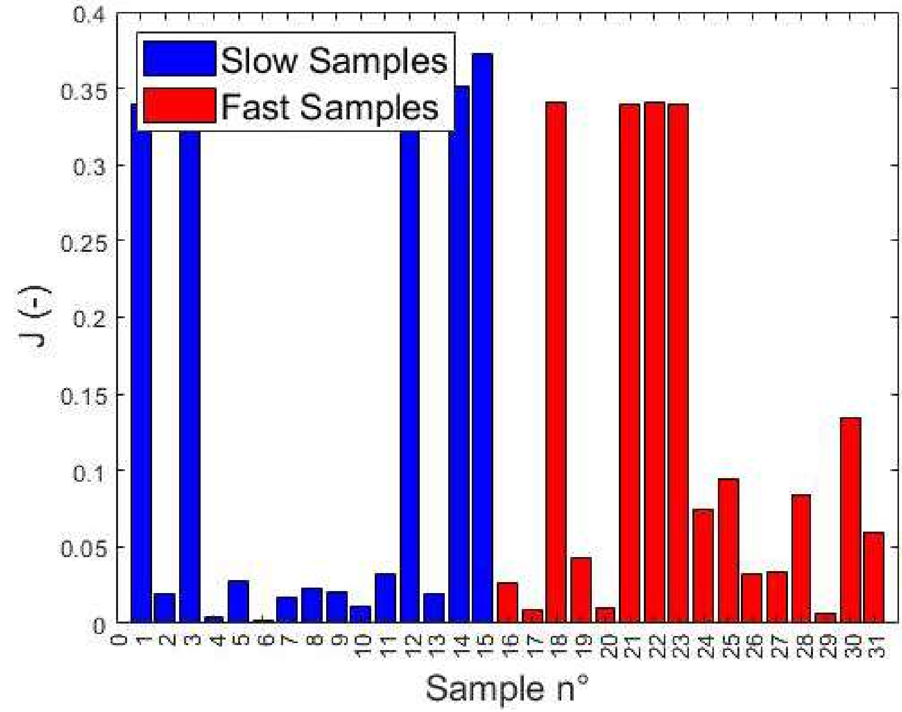

Figure F.12: Cost function value at the solution for each sample. Blue corresponds to samples tested with a slow strain-rate loading and red to the samples tested with fast strain-rate loading.

References

[1] A. Gefen, D. M. Brienza, J. Cuddigan, E. Haesler, J. Kottner, Our contemporary understanding of the aetiology of pressure ulcers/pressure injuries, International Wound Journal n/a (2021). URL: https://onlinelibrary.wiley.com/doi/abs/10.1111/iwj.13667. doi:https://doi.org/10.1111/iwj.13667.

[2] A. Gefen, P. Alves, G. Ciprandi, F. Coyer, C. T. Milne, K. Ousey, N. Ohura, N. Waters, P. Worsley, J. Black, M. Barakat-Johnson, D. Beeckman, J. Fletcher, H. Kirkland-Kyhn, N. A. Lahmann, Z. Moore, Y. Payan, A.-B. Schlüer, Device-related pressure ulcers: SECURE prevention, Journal of Wound Care 29 (2020) S1–S52. URL: https://doi.org/10.12968/jowc.2020.29.sup2a.s1. doi:10.12968/jowc.2020.29.sup2a.s1.

[3] G. Bennett, C. Dealey, J. Posnett, The cost of pressure ulcers in the UK, Age and Ageing 33 (2004) 230–235. URL: https://doi.org/10.1093/ageing/afh086. doi:10.1093/ageing/afh086. arXiv:https://academic.oup.com/ageing/article-pdf/33/3/

[4] K. Ceelen, A. Stekelenburg, S. Loerakker, G. Strijkers, D. Bader, K. Nicolay, F. Baaijens, C. Oomens, Compression-induced damage and internal tissue strains are related, Journal of Biomechanics 41 (2008) 3399–3404. URL: https://doi.org/10.1016/j.jbiomech.2008.09.016. doi:10.1016/j.jbiomech.2008.09.016.

[5] S. Loerakker, E. Manders, G. J. Strijkers, K. Nicolay, F. P. T. Baaijens, D. L. Bader, C. W. J. Oomens, The effects of deformation, ischemia, and reperfusion on the development of muscle damage during prolonged loading, Journal of Applied Physiology 111 (2011) 1168–1177. URL: https://doi.org/10.1152/japplphysiol.00389.2011. doi:10.1152/japplphysiol.00389.2011.

[6] A. Stekelenburg, C. W. J. Oomens, G. J. Strijkers, K. Nicolay, D. L. Bader, Compression-induced deep tissue injury examined with magnetic resonance imaging and histology, Journal of Applied Physiology 100 (2006) 1946–1954.

URL: https://doi.org/10.1152/japplphysiol.00889.2005. doi:10.1152/japplphysiol.00889.2005.

[7] B. J. van Nierop, A. Stekelenburg, S. Loerakker, C. W. Oomens, D. Bader, G. J. Strijkers, K. Nicolay, Diffusion of water in skeletal muscle tissue is not influenced by compression in a rat model of deep tissue injury, Journal of Biomechanics 43 (2010) 570–575. URL: https://doi.org/10.1016/j.jbiomech.2009.07.043. doi:10.1016/j.jbiomech.2009.07.043.

[8] W. A. Traa, M. C. van Turnhout, J. L. Nelissen, G. J. Strijkers, D. L. Bader, C. W. Oomens, There is an individual tolerance to mechanical loading in compression induced deep tissue injury, Clinical Biomechanics 63 (2019) 153–160. URL: https://doi.org/10.1016/j.clinbiomech.2019.02.015. doi:10.1016/j.clinbiomech.2019.02.015.

[9] S. Loerakker, A. Stekelenburg, G. J. Strijkers, J. J. M. Rijpkema, F. P. T. Baaijens, D. L. Bader, K. Nicolay, C. W. J. Oomens, Temporal effects of mechanical loading on deformation-induced damage in skeletal muscle tissue, Annals of Biomedical Engineering 38 (2010) 2577–2587. URL: https://doi.org/10.1007/s10439-010-0002-x. doi:10.1007/s10439-010-0002-x.

[10] E. Linder-Ganz, G. Yarnitzky, Z. Yizhar, I. Siev-Ner, A. Gefen, Real-time finite element monitoring of sub-dermal tissue stresses in individuals with spinal cord injury: Toward prevention of pressure ulcers, Annals of Biomedical Engineering 37 (2008) 387–400. URL: https://doi.org/10.1007/s10439-008-9607-8. doi:10.1007/s10439-008-9607-8.

[11] E. Linder-Ganz, N. Shabshin, Y. Itzchak, A. Gefen, Assessment of mechanical conditions in sub-dermal tissues during sitting: A combined experimental-MRI and finite element approach, Journal of Biomechanics 40 (2007) 1443–1454. URL: https://doi.org/10.1016/j.jbiomech.2006.06.020. doi:10.1016/j.jbiomech.2006.06.020.

[12] E. Linder-Ganz, S. Engelberg, M. Scheinowitz, A. Gefen, Pressure–time cell death threshold for albino rat skeletal muscles as related to pres-

sure sore biomechanics, Journal of Biomechanics 39 (2006) 2725–2732. URL: https://doi.org/10.1016/j.jbiomech.2005.08.010. doi:10.1016/j.jbiomech.2005.08.010.

[13] V. Luboz, M. Bailet, C. B. Grivot, M. Rochette, B. Diot, M. Bucki, Y. Payan, Personalized modeling for real-time pressure ulcer prevention in sitting posture, Journal of Tissue Viability 27 (2018) 54–58. URL: https://doi.org/10.1016/j.jtv.2017.06.002. doi:10.1016/j.jtv.2017.06.002.

[14] K. M. Moerman, M. van Vijven, L. R. Solis, E. E. van Haaften, A. C. Y. Loenen, V. K. Mushahwar, C. W. J. Oomens, On the importance of 3d, geometrically accurate, and subject-specific finite element analysis for evaluation of in-vivo soft tissue loads, Computer Methods in Biomechanics and Biomedical Engineering 20 (2016) 483–491. URL: https://doi.org/10.1080/10255842.2016.1250259. doi:10.1080/10255842.2016.1250259.

[15] A. Macron, H. Pillet, J. Doridam, A. Verney, P.-Y. Rohan, Development and evaluation of a new methodology for the fast generation of patient-specific finite element models of the buttock for sitting-acquired deep tissue injury prevention, Journal of Biomechanics 79 (2018) 173–180. URL: https://doi.org/10.1016/j.jbiomech.2018.08.001. doi:10.1016/j.jbiomech.2018.08.001.

[16] M. Bucki, V. Luboz, A. Perrier, E. Champion, B. Diot, N. Vuillerme, Y. Payan, Clinical workflow for personalized foot pressure ulcer prevention, Medical Engineering & Physics 38 (2016) 845–853. URL: https://doi.org/10.1016/j.medengphy.2016.04.017. doi:10.1016/j.medengphy.2016.04.017.

[17] S. Niroomandi, A. Perrier, M. Bucki, Y. Payan, Real-time computer modeling in prevention of foot pressure ulcer using patient-specific finite element model and model order reduction techniques, in: Innovations and Emerging Technologies in Wound Care, Elsevier, 2020, pp. 87–102. URL: https://doi.org/10.1016/b978-0-12-815028-3.00005-5. doi:10.1016/b978-0-12-815028-3.00005-5.

[18] W. van Zwam, M. van Turnhout, C. Oomens, Risk factors for developing heel ulcers for bedridden patients: A fi-

nite element study, Clinical Biomechanics 78 (2020) 105094. URL: https://doi.org/10.1016/j.clinbiomech.2020.105094. doi:10.1016/j.clinbiomech.2020.105094.

[19] S. Portnoy, I. Siev-Ner, N. Shabshin, A. Kristal, Z. Yizhar, A. Gefen, Patient-specific analyses of deep tissue loads post transtibial amputation in residual limbs of multiple prosthetic users, Journal of Biomechanics 42 (2009) 2686–2693. URL: https://doi.org/10.1016/j.jbiomech.2009.08.019. doi:10.1016/j.jbiomech.2009.08.019.

[20] A. Dickinson, J. Steer, P. Worsley, Finite element analysis of the amputated lower limb: A systematic review and recommendations, Medical Engineering & Physics 43 (2017) 1–18. URL: https://doi.org/10.1016/j.medengphy.2017.02.008. doi:10.1016/j.medengphy.2017.02.008.

[21] E. Ramasamy, O. Avci, B. Dorow, S.-Y. Chong, L. Gizzi, G. Steidle, F. Schick, O. Röhrle, An efficient modelling-simulation-analysis workflow to investigate stump-socket interaction using patient-specific, three-dimensional, continuum-mechanical, finite element residual limb models, Frontiers in Bioengineering and Biotechnology 6 (2018). URL: https://doi.org/10.3389/fbioe.2018.00126. doi:10.3389/fbioe.2018.00126.

[22] R. M. A. Al-Dirini, M. P. Reed, J. Hu, D. Thewlis, Development and validation of a high anatomical fidelity FE model for the buttock and thigh of a seated individual, Annals of Biomedical Engineering 44 (2016) 2805–2816. URL: https://doi.org/10.1007/s10439-016-1560-3. doi:10.1007/s10439-016-1560-3.

[23] M. Van Loocke, C. Simms, C. Lyons, Viscoelastic properties of passive skeletal muscle in compression—cyclic behaviour, Journal of Biomechanics 42 (2009) 1038–1048. URL: https://doi.org/10.1016/j.jbiomech.2009.02.022. doi:10.1016/j.jbiomech.2009.02.022.

[24] C. K. Simms, M. V. Loocke, C. G. Lyons, SKELETAL MUSCLE IN COMPRESSION: MODELING APPROACHES FOR THE PASSIVE MUSCLE BULK, International Journal

for Multiscale Computational Engineering 10 (2012) 143–154. URL: https://doi.org/10.1615/intjmultcompeng.2011002419. doi:10.1615/intjmultcompeng.2011002419.

[25] B. B. Wheatley, R. B. Pietsch, T. L. H. Donahue, L. N. Williams, Fully non-linear hyper-viscoelastic modeling of skeletal muscle in compression, Computer Methods in Biomechanics and Biomedical Engineering 19 (2015) 1181–1189. URL: https://doi.org/10.1080/10255842.2015.1118468. doi:10.1080/10255842.2015.1118468.

[26] G. Sjogaard, B. Saltin, Extra- and intracellular water spaces in muscles of man at rest and with dynamic exercise, American Journal of Physiology-Regulatory, Integrative and Comparative Physiology 243 (1982) R271–R280. URL: https://doi.org/10.1152/ajpregu.1982.243.3.R271. doi:10.1152/ajpregu.1982.243.3.R271, pMID: 7114288.

[27] O. A. Gimnich, J. Singh, J. Bismuth, D. J. Shah, G. Brunner, Magnetic resonance imaging based modeling of microvascular perfusion in patients with peripheral artery disease, Journal of Biomechanics 93 (2019) 147–158. URL: https://doi.org/10.1016/j.jbiomech.2019.06.025. doi:10.1016/j.jbiomech.2019.06.025.

[28] M. Argoubi, A. Shirazi-Adl, Poroelastic creep response analysis of a lumbar motion segment in compression, Journal of Biomechanics 29 (1996) 1331–1339. URL: https://doi.org/10.1016/0021-9290(96)00035-8. doi:10.1016/0021-9290(96)00035-8.

[29] M. Peyrounette, Y. Davit, M. Quintard, S. Lorthois, Multiscale modelling of blood flow in cerebral microcirculation: Details at capillary scale control accuracy at the level of the cortex, PLOS ONE 13 (2018) e0189474. URL: https://doi.org/10.1371/journal.pone.0189474. doi:10.1371/journal.pone.0189474.

[30] J. Siddique, A. Ahmed, A. Aziz, C. Khalique, A review of mixture theory for deformable porous media and applications, Applied Sciences 7 (2017) 917. URL: https://doi.org/10.3390/app7090917. doi:10.3390/app7090917.

[31] M. Hosseini-Farid, M. Ramzanpour, J. McLean, M. Ziejewski, G. Karami, A poro-hyper-viscoelastic rate-dependent constitutive modeling for the analysis of brain tissues, Journal of the Mechanical Behavior of Biomedical Materials 102 (2020) 103475. URL: https://doi.org/10.1016/j.jmbbm.2019.103475. doi:10.1016/j.jmbbm.2019.103475.

[32] G. Franceschini, D. Bigoni, P. Regitnig, G. Holzapfel, Brain tissue deforms similarly to filled elastomers and follows consolidation theory, Journal of the Mechanics and Physics of Solids 54 (2006) 2592–2620. URL: https://doi.org/10.1016/j.jmps.2006.05.004. doi:10.1016/j.jmps.2006.05.004.

[33] G. Sciumè, D. P. Boso, W. G. Gray, C. Cobelli, B. A. Schrefler, A two-phase model of plantar tissue: a step toward prediction of diabetic foot ulceration, International Journal for Numerical Methods in Biomedical Engineering 30 (2014) 1153–1169. URL: https://onlinelibrary.wiley.com/doi/abs/10.1002/cnm.2650. doi:https://doi.org/10.1002/cnm.2650. arXiv:https://onlinelibrary.wiley.com/doi/pdf

[34] S. Urcun, P.-Y. Rohan, W. Skalli, P. Nassoy, S. P. A. Bordas, G. Sciumè, Digital twinning of cellular capsule technology: Emerging outcomes from the perspective of porous media mechanics, PLOS ONE 16 (2021) 1–30. URL: https://doi.org/10.1371/journal.pone.0254512. doi:10.1371/journal.pone.0254512.

[35] G. Sciumè, S. Shelton, W. G. Gray, C. T. Miller, F. Hussain, M. Ferrari, P. Decuzzi, B. A. Schrefler, A multiphase model for three-dimensional tumor growth, New Journal of Physics 15 (2013) 015005. URL: https://doi.org/10.1088/1367-2630/15/1/015005. doi:10.1088/1367-2630/15/1/015005.

[36] G. Sciumè, Mechanistic modeling of vascular tumor growth: an extension of biot's theory to hierarchical bi-compartment porous medium systems, Acta Mechanica 232 (2021) 1445–1478. URL: https://doi.org/10.1007/s00707-020-02908-z. doi:10.1007/s00707-020-02908-z.

[37] W. G. Gray, C. T. Miller, Introduction to the Thermodynamically Constrained Averaging Theory for Porous Medium

Systems, Springer International Publishing, 2014. URL: https://doi.org/10.1007/978-3-319-04010-3. doi:10.1007/978-3-319-04010-3.

[38] P. Mascheroni, C. Stigliano, M. Carfagna, D. P. Boso, L. Preziosi, P. Decuzzi, B. A. Schrefler, Predicting the growth of glioblastoma multiforme spheroids using a multiphase porous media model, Biomechanics and Modeling in Mechanobiology 15 (2016) 1215–1228. URL: https://doi.org/10.1007/s10237-015-0755-0. doi:10.1007/s10237-015-0755-0.

[39] A. J. Vaidya, B. B. Wheatley, An experimental and computational investigation of the effects of volumetric boundary conditions on the compressive mechanics of passive skeletal muscle, Journal of the Mechanical Behavior of Biomedical Materials 102 (2020) 103526. URL: https://doi.org/10.1016/j.jmbbm.2019.103526. doi:10.1016/j.jmbbm.2019.103526.

[40] M. Viceconti, S. Olsen, L.-P. Nolte, K. Burton, Extracting clinically relevant data from finite element simulations 20 (2005) 451–454. URL: https://doi.org/10.1016/j.clinbiomech.2005.01.010. doi:10.1016/j.clinbiomech.2005.01.010.

[41] I. Abaqus, Abaqus documentation, Version 6 (2014) 1–5.

[42] D. A. Sleboda, T. J. Roberts, Incompressible fluid plays a mechanical role in the development of passive muscle tension, Biology Letters 13 (2017) 20160630. URL: https://doi.org/10.1098/rsbl.2016.0630. doi:10.1098/rsbl.2016.0630.

[43] B. B. Wheatley, G. M. Odegard, K. R. Kaufman, T. L. H. Donahue, A validated model of passive skeletal muscle to predict force and intramuscular pressure, Biomechanics and Modeling in Mechanobiology 16 (2016) 1011–1022. URL: https://doi.org/10.1007/s10237-016-0869-z. doi:10.1007/s10237-016-0869-z.

[44] C. Oomens, W. Zenhorst, M. Broek, B. Hemmes, M. Poeze, P. Brink, D. Bader, A numerical study to analyse the risk for pressure ulcer development on a spine board 28 (2013) 736–742. URL: https://doi.org/10.1016/j.clinbiomech.2013.07.005. doi:10.1016/j.clinbiomech.2013.07.005.

[45] W. A. Traa, M. C. van Turnhout, K. M. Moerman, J. L. Nelissen, A. J. Nederveen, G. J. Strijkers, D. L. Bader, C. W. J. Oomens, MRI based 3d finite element modelling to investigate deep tissue injury, Computer Methods in Biomechanics and Biomedical Engineering 21 (2018) 760–769. URL: `https://doi.org/10.1080/10255842.2018.1517868`. doi:10.1080/10255842.2018.1517868.

[46] W. Lee, B. H. Won, S. W. Cho, Finite element modeling for predicting the contact pressure between a foam mattress and the human body in a supine position 20 (2016) 104–117. URL: `https://doi.org/10.1080/10255842.2016.1203421`. doi:10.1080/10255842.2016.1203421.

[47] M. Verver, J. van Hoof, C. Oomens, J. Wismans, F. Baaijens, A finite element model of the human buttocks for prediction of seat pressure distributions 7 (2004) 193–203. URL: `https://doi.org/10.1080/10255840410001727832`. doi:10.1080/10255840410001727832.

[48] A. Levy, K. Kopplin, A. Gefen, Simulations of skin and subcutaneous tissue loading in the buttocks while regaining weight-bearing after a push-up in wheelchair users 28 (2013) 436–447. URL: `https://doi.org/10.1016/j.jmbbm.2013.04.015`. doi:10.1016/j.jmbbm.2013.04.015.

[49] R. Sopher, J. Nixon, C. Gorecki, A. Gefen, Exposure to internal muscle tissue loads under the ischial tuberosities during sitting is elevated at abnormally high or low body mass indices 43 (2010) 280–286. URL: `https://doi.org/10.1016/j.jbiomech.2009.08.021`. doi:10.1016/j.jbiomech.2009.08.021.

[50] T. Zeevi, A. Levy, N. Brauner, A. Gefen, Effects of ambient conditions on the risk of pressure injuries in bedridden patients-multi-physics modelling of microclimate 15 (2017) 402–416. URL: `https://doi.org/10.1111/iwj.12877`. doi:10.1111/iwj.12877.

[51] L.-L. Gras, D. Mitton, N. Crevier-Denoix, S. Laporte, The nonlinear response of a muscle in transverse compression: assessment of geometry influence using a finite element model, Computer Methods in Biomechanics and Biomedical Engineering 15 (2012)

13–21. URL: https://doi.org/10.1080/10255842.2011.564162. doi:10.1080/10255842.2011.564162.

[52] V. Klika, E. A. Gaffney, Y.-C. Chen, C. P. Brown, An overview of multiphase cartilage mechanical modelling and its role in understanding function and pathology, Journal of the Mechanical Behavior of Biomedical Materials 62 (2016) 139–157. URL: https://www.sciencedirect.com/science/article/pii/S1751616116301047. doi:https://doi.org/10.1016/j.jmbbm.2016.04.032.

[53] S. C. Cowin, Bone poroelasticity, Journal of Biomechanics 32 (1999) 217–238. URL: https://www.sciencedirect.com/science/article/pii/S0021929098001614. doi:https://doi.org/10.1016/S0021-9290(98)00161-4.

[54] C. Hellmich, F.-J. Ulm, Drained and undrained poroelastic properties of healthy and pathological bone: A poro-micromechanical investigation 58 (2005) 243–268. URL: https://doi.org/10.1007/s11242-004-6298-y. doi:10.1007/s11242-004-6298-y.

[55] B. B. Wheatley, G. M. Odegard, K. R. Kaufman, T. L. H. Donahue, A case for poroelasticity in skeletal muscle finite element analysis: experiment and modeling, Computer Methods in Biomechanics and Biomedical Engineering 20 (2016) 598–601. URL: https://doi.org/10.1080/10255842.2016.1268132. doi:10.1080/10255842.2016.1268132.

[56] G. Sjogaard, B. Saltin, Extra- and intracellular water spaces in muscles of man at rest and with dynamic exercise 243 (1982) R271–R280. URL: https://doi.org/10.1152/ajpregu.1982.243.3.r271. doi:10.1152/ajpregu.1982.243.3.r271.

[57] M. A. Soltz, G. A. Ateshian, Experimental verification and theoretical prediction of cartilage interstitial fluid pressurization at an impermeable contact interface in confined compression, Journal of Biomechanics 31 (1998) 927–934. URL: https://doi.org/10.1016/s0021-9290(98)00105-5. doi:10.1016/s0021-9290(98)00105-5.

[58] Tavenas, F., Brucy, M., Magnan, J.-P., La Rochelle, P., Roy, M., Analyse critique de la théorie de consolidation unidimensionnelle de terzaghi, Rev. Fr. Geotech. (1979) 29–43. URL: https://doi.org/10.1051/geotech/1979007029. doi:10.1051/geotech/1979007029.